JOURNAL OF GEOPHYSICAL RESEARCH, VOL. 103, NO. E11, PAGES 25,789–25,807, OCTOBER 25, 1998

Effect of surface roughness on bidirectional reflectance of Antarctic snow

Stephen G. Warren and Richard E. Brandt
Department of Atmospheric Sciences, University of Washington, Seattle

Patricia O'Rawe Hinton
Science Applications International Corporation, Hampton, Virginia

Abstract. The angular pattern of sunlight reflected by snow is altered by surface roughness, which in the interior of Antarctica is usually in the form of meter-scale longitudinal erosional features (sastrugi), whose axes align with the direction of strong winds. The bidirectional reflectance distribution function (BRDF) changes over the course of a day as the solar azimuth changes relative to the sastrugi axis. The normalized BRDF, or "anisotropic reflectance factor" R, was measured at South Pole Station from a 22-m tower at 600, 660, and 900 nm wavelengths. The R pattern was similar at the three wavelengths; it probably varies little from 300 to 900 nm. Measurements were made at solar zenith angles θ_o from 67° to 90°, over the full range of viewing zenith angle (θ_r), azimuth angle between Sun and view (ϕ), and azimuth angle between Sun and sastrugi (ϕ_{sas}). Variation of R with ϕ_{sas} was notable; sastrugi oriented perpendicular to the solar beam cause a reduction of the forward peak, and sastrugi at an oblique angle cause R to lose its symmetry about the solar azimuth. However, the effects of sastrugi are mostly restricted to large viewing zenith angles, so remote sensing of albedo and atmospheric properties can be carried out accurately without knowledge of sastrugi height and orientation if only near-nadir views are used. This recommendation is opposite that for observations of broken clouds over dark surfaces, for which large θ_r is preferred. A parameterization of R is developed, valid for viewing angles $\theta_r \leq 50°$. Sastrugi can cause a reduction of the snow albedo by altering the angle of incidence and by trapping of photons. For the small sastrugi of the Antarctic Plateau, the albedo is unaffected at visible wavelengths but can be reduced by a few percent at near-infrared wavelengths when the Sun is low.

1. Introduction

The use of reflected sunlight for remote sensing by satellite of the atmosphere above a snow surface, and of the snow surface itself, requires knowledge of how the reflected radiation is distributed with angle. This is because a narrow-field-of-view sensor on a satellite measures the reflected radiance only in a particular direction, and that radiance may be more or less than the average radiance. The function that describes the distribution of reflected radiance with angle, called the bidirectional reflectance distribution function, is a function of four angles: incoming (solar) zenith and azimuth (θ_o, ϕ_o), and outgoing (reflected) zenith and azimuth (θ_r, ϕ_r) (Figure 1). For areal or temporal averages of many natural surfaces, only three angles are needed to describe the function because only the difference between the two azimuths (ϕ_r-ϕ_o) is important, not their individual values. Indeed, the reflectance pattern is usually symmetric about the solar azimuth as well, so that it depends on just the absolute value of the difference, $|\phi_r-\phi_o|$. In large areas of the polar regions, however, both azimuth angles may need to be specified relative to the azimuth of the prevailing wind because the snow is eroded by the wind into meter-scale longitudinal dunes called sastrugi [*Armstrong et al.*, 1966; *Mather,* 1962].

Sastrugi occur on ice sheets, ice caps, sea ice, and tundra. They are most prominent where ice-sheet surfaces are exposed to persistent strong winds from a single direction, as on the "Slope" of the ice sheet around the perimeter of East Antarctica. They have been used to infer the directions of prevailing winds over the continent [*Parish and Bromwich,* 1987]. On the high plateau of East Antarctica, where our measurements were taken, the winds are weaker and more variable, and the sastrugi, though always present, are not as large as on the Slope. On the plateau their lengths are typically a few meters, widths 1 m, and heights 0.1-0.5 m. They can on occasion be completely eroded and reformed in a single storm, so a particular orientation and height cannot be assumed for interpretation of satellite radiances. Sometimes there is not a single orientation of sastrugi, but rather two or three sets of sastrugi crossing each other and forming a network of ridges (Figure 2). On the Antarctic Ice Sheet, sastrugi undergo a seasonal cycle, growing in winter and decaying in summer, for reasons explained by *Gow* [1965] and *Weller* [1969]. The original Russian word "zastrugi" is a collective noun, lacking singular and plural forms. In accordance with usage now becoming established in English, however, we use "sastrugi" as a plural noun, "sastruga" as a

Paper number 98JE01898.
0148-0227/98/98JE-01898$09.00

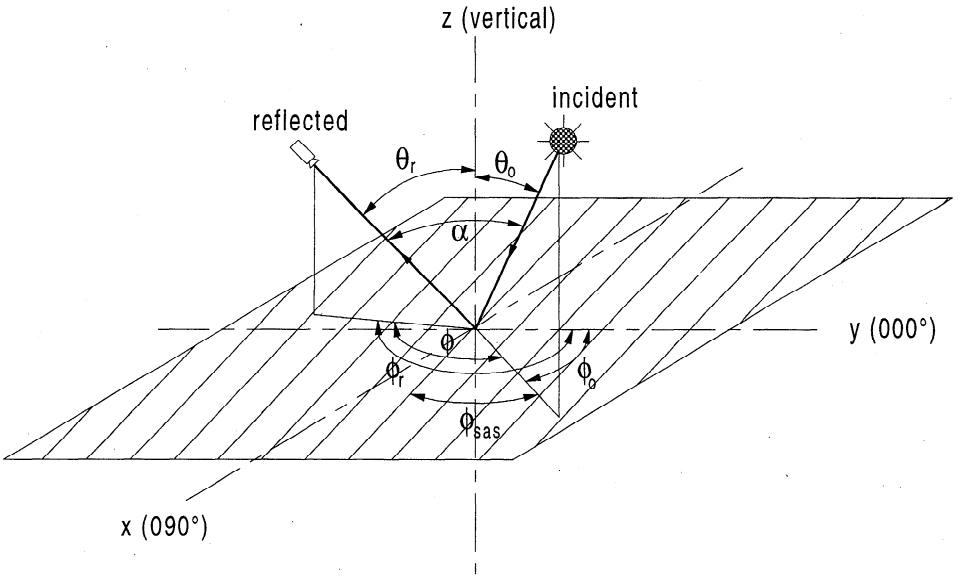

Figure 1. Definition of incident (solar) zenith angle θ_o, viewing (reflectance) zenith angle θ_r, solar azimuth angle ϕ_o, viewing azimuth angle ϕ_r, relative viewing azimuth ϕ, relative sastrugi azimuth ϕ_{sas}, and phase angle α.

singular noun to mean a single element in a field of sastrugi, and "sastrugied" as an adjective, from the Russian "zastruzhennyy."

The bidirectional reflectance of sastrugi fields can differ markedly from that of a flat snow surface, particularly at large viewing zenith angles θ_r. The bidirectional reflectance pattern of flat snow exhibits a peak in the forward direction, but this peak is diminished when the solar beam is oriented perpendicular to the sastrugi. In extreme cases of steep-sided sastrugi a view of the sastrugi field in the direction toward the Sun can consist mostly of shadows.

It turns out, however, that sastrugi have much less effect on the brightness of light reflected into directions near the vertical. In this paper we therefore investigate the possibility that there is a range of viewing angles for which remote sensing of albedo and atmospheric constituents can be carried out accurately over sastrugi fields without knowledge of the sastrugi heights and orientations.

2. Terminology

The ratio of the spectral flux (W $m^{-2}\mu m^{-1}$) reflected into the entire upward hemisphere, to the incident flux, which may be coming down from a single direction (the Sun) is the directional-hemispherical spectral reflectance, often simply called the (spectral) albedo, A. In planetary studies, A is sometimes called the spherical albedo, the hemispherical albedo, or the plane albedo. We will use the symbol A for albedo, and A_s for surface albedo. The bidirectional reflectance distribution function (BRDF), given the symbol ρ

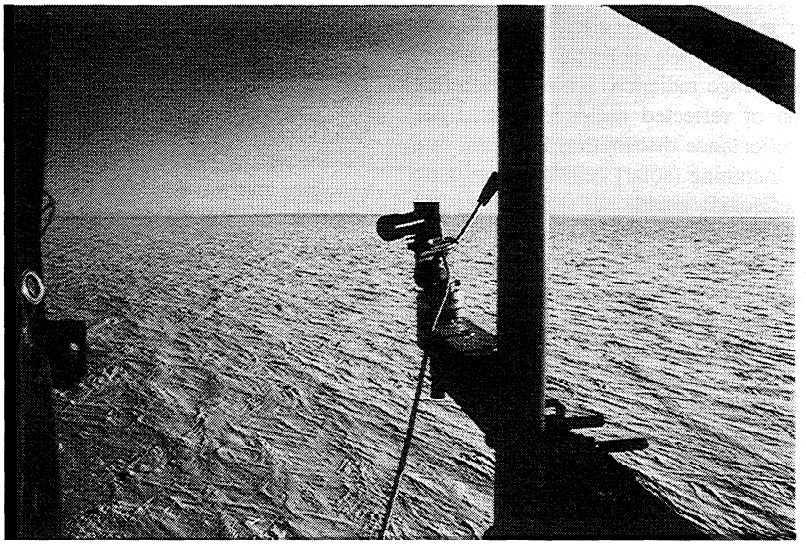

Figure 2. Photograph taken from the 22-m tower at South Pole Station showing the goniometer and radiance probe, and the snow surface with sastrugi.

(units sr^{-1}), is the ratio of the radiance (W m^{-2} sr^{-1} μm^{-1}) reflected into a particular direction, to the incident flux. The albedo A can therefore be expressed as an integral of ρ over the upward hemisphere, weighted by the cosine of the reflectance zenith angle θ_r:

$$A(\theta_o) = \int_0^{2\pi} \int_0^{\pi/2} \rho(\theta_o, \theta_r, \phi_r - \phi_o) \cos\theta_r \sin\theta_r \, d\theta_r \, d\phi_r. \quad (1)$$

Because of Earth's curvature, for satellite views the reflectance zenith angle θ_r (the angle at which photons emerge from the snow surface) must be distinguished from the viewing nadir angle (the angle of view outward from the vertically downward, or nadir, direction). However, the field measurements described in this paper were made only 22 m above the snow surface, for which these two angles are equal. We will therefore often call this angle the viewing zenith angle.

Comparison of BRDF patterns is facilitated by nondimensionalizing and normalizing them. Following *Suttles et al.* [1988], we therefore define the anisotropic reflectance factor (R) as

$$R(\theta_o, \theta_r, \phi_r - \phi_o) \equiv \frac{\pi}{A} \rho(\theta_o, \theta_r, \phi_r - \phi_o). \quad (2)$$

This function has the property that its average value over the upward hemisphere (weighted by its contribution to the upward flux, proportional to $\cos\theta_r$) is unity:

$$\overline{R} = \frac{1}{\pi} \int_0^{2\pi} \int_0^{\pi/2} R(\theta_o, \theta_r, \phi_r - \phi_o) \cos\theta_r \sin\theta_r \, d\theta_r \, d\phi_r = 1. \quad (3)$$

Two special cases of surface reflectance patterns are those of (1) a "Lambertian" surface, in which the reflected brightness is the same at all viewing angles in the upward hemisphere, $R(\theta_r, \phi_r) = 1$, and (2) a mirror, for which R is a delta function.

The only planetary surface that approaches the behavior of a mirror is a calm water surface. Other natural surfaces are commonly represented (as the lower boundary condition in climate models or in atmospheric radiation models) as Lambertian reflectors, so it is useful to think of a Lambertian surface as a reference standard, and to examine deviations from Lambertian behavior. *Taylor and Stowe* [1984a,b] used observations from the Nimbus 7 satellite to derive empirical R patterns for use in the Earth Radiation Budget Experiment (ERBE) for ocean, snow, ice, snow-free land, and clouds. Of all these scenes, snow was the closest to Lambertian in its reflectance pattern, but it still exhibited substantial deviations from Lambertian behavior. Taylor and Stowe's results may be expected to differ from R patterns measured at the surface because (1) Taylor and Stowe used broadband detectors and thus obtained an average over the solar spectrum, (2) their R patterns are not for the snow surface but rather for the snow-atmosphere system, which includes Rayleigh scattering and ozone absorption, and (3) they have averaged over sastrugi orientations.

3. Factors Affecting Bidirectional Reflectance of Snow

3.1. Single-Scattering Phase Function

Snow grains are typically 50-1000 μm in radius, much larger than the wavelengths of solar radiation, so their phase functions are strongly forward peaked (i.e., during scattering events, most incident photons are deflected only slightly). The single-scattering asymmetry factor g exceeds 0.88 for all solar wavelengths [*Wiscombe and Warren,* 1980, Figure 4]. The consequence for the BRDF is that when the Sun is low, the photons that escape the snowpack after one or a few scattering events tend to emerge near the limb ($\theta_r \approx 90^0$) and close to the forward azimuth ($\phi_r \approx \phi_o + \pi$).

This behavior was demonstrated nearly half a century ago by *Middleton and Mungall* [1952], who were the first to show that snow reflectance was non-Lambertian. Using an artificial light source to illuminate fresh snow at night in Canada, they observed a peak of brightness in the forward direction that increased in strength as the zenith angle of illumination increased. This peak was not centered at the mirror angle, as they had expected, but rather at near-limb viewing, a nadir angle of nearly 90^0.

3.2. Solar Zenith Angle

At wavelengths where snow exhibits significant absorption, the albedo A_s depends on θ_o, with higher albedo at low sun [*Wiscombe and Warren,* 1980, Figure 11]. Most of the results shown in this paper are for wavelengths 600-660 nm, where there is little absorption and A_s is so high that it does not depend on θ_o. However, the bidirectional reflectance R does depend on θ_o, even though A_s does not.

When the Sun is high above the horizon, the forward scattered photons penetrate deeply into the snow and require many scattering events to be redirected upward and eventually escape the snowpack. The emerging photons are therefore distributed more uniformly with angle into the upward hemisphere than is the case for lower solar elevations. The progression from a nearly Lambertian R for high Sun to a strongly forward-peaked R for low Sun was demonstrated by *Dirmhirn and Eaton* [1975] for melting snow on a spring afternoon in Utah, using a broadband detector. Their measurements, as well as those of *Middleton and Mungall* [1952] and others, were reviewed by *Warren* [1982].

3.3. Snow Grain Size

The average snow grain size (or volume-to-surface ratio) normally increases as the snow ages, due to "destructive metamorphism," which occurs even in cold snow but proceeds much more rapidly in melting snow [*LaChapelle,* 1969]. This has two consequences, both of which cause increased anisotropy of the BRDF. First, the forward peak of the single-scattering phase function becomes narrower and stronger as the snow grain size increases [*Wiscombe and Warren,* 1980, Figure 4; *Hansen and Travis,* 1974, Figure 5a]. As a result, the forward peak of the multiple-scattering BRDF is more pronounced for larger grains. Second, photons are more likely to be absorbed in coarse-grained snow than in fine-grained snow because they have to pass through longer paths in ice between opportunities for scattering at air-ice interfaces. This means that the photons that do emerge from coarse-grained snow are predominantly those that have undergone only a few scattering events, so that the BRDF more closely resembles the highly peaked single-scattering phase function and is less diffuse than for fine-grained snow. However, this second reason does not apply to visible wavelengths, where the absorption coefficient of ice is extremely small.

The effect of grain growth on R was demonstrated for visible wavelengths by *Steffen* [1987], who sampled R at 15° intervals in θ_r and ϕ_r for snow of three ages: 5, 24, and 72 hours. The pattern became more anisotropic as the snow aged, as expected.

3.4. Absorption Coefficient of Ice

The absorption coefficient of ice increases with wavelength λ by 5 orders of magnitude across the solar spectrum from λ=0.5 μm to λ=2 μm. Correspondingly, the multiple-scattering survival probability of photons (i.e., the albedo) decreases with wavelength. At λ=2 μm the mean free path of a photon before absorption in ice is only 0.1 mm, so the few photons that survive interaction with the snow have mostly escaped after just one scattering event, and R resembles the single-scattering phase function.

At visible wavelengths, by contrast, the reflected light consists mostly of photons that were scattered numerous times in the snow, so the reflectance pattern is more diffuse. This variation of R with wavelength was illustrated by *Li* [1982], who computed the BRDF at 0.5 μm and 1.2 μm using an adding-doubling radiative transfer model.

Small targets of flat snow in Antarctica were studied by *Carlson and Arakelian* [1993] and *Arakelian* [1995] with an instrument located 0.3 m above the snow surface, at 14 different wavelengths from 0.5 to 2.4 μm. Reflectance measured in the "principal plane" (perpendicular to the snow surface and intersecting the Sun) became more anisotropic, with a more pronounced forward peak, as the absorption coefficient increased: the smallest forward peak (relative to the average brightness in the principal plane) was at λ=0.5 μm, where the absorption is least and albedo is high (A_s≈0.98 [*Grenfell et al.,* 1994]), and the most anisotropic pattern was at λ=2.0 μm, where ice absorption is at a maximum and albedo is minimum (A_s<0.1). At λ=2.0 μm, most of the incident photons were absorbed, but the few that did escape exited in the forward direction near the limb.

Across the visible spectrum, the absorption coefficient does vary, but it is everywhere so small that almost no absorption occurs during transit of light through individual snow grains. Correspondingly, measurements over snow from aircraft by *Griggs and Marggraf* [1967] showed that R (sampled at a few angles) was independent of wavelength from 440 to 960 nm. *Winther* [1994, Figure 3] found the variation of R with viewing angle in the principal plane to be nearly independent of wavelength from 380 to 700 nm, but anisotropy increased from 700 to 900 nm.

3.5. Surface Roughness

The importance of "macroscopic" surface roughness (i.e., on scales much larger than the wavelength of light) in bidirectional reflectance spectroscopy has long been recognized in planetary astronomy, to explain the variation of brightness with phase angle and the variation of brightness across the face of a planet. At large solar zenith angles, surface roughness enhances the backscatter by altering the angle of incidence, and reduces the forward scatter by casting shadows. These effects are discussed by *Hapke* [1971], who also derived a model for a planetary surface with randomly oriented roughness [*Hapke*, 1984]. A lucid explanation of effects of surface roughness was given by *Nayar and Oren* [1995], who also offered a simple approximation to their complex model. Both their model and Hapke's model assume that the roughness features are randomly oriented, so they cannot be used to explain the variation of R with ϕ_{sas} which we observe.

The importance of surface roughness for snow was recognized by *Kuhn* [1974, 1985], who pioneered the study of its effect on BRDF. Snow surfaces can exhibit many different forms of roughness, including suncups and penitents [*Post and LaChapelle,* 1971; *Lliboutry,* 1954; *Rhodes et al.,* 1987], but the most important by far is sastrugi, which cover vast areas of the polar regions. *Kuhn* [1974] demonstrated a weakening of the forward peak due to shading when the solar beam was oriented perpendicular to the sastrugi.

The effect of sastrugi on bidirectional reflectance and albedo has been modeled by *O'Rawe* [1991] and *Leroux and Fily* [this issue], using idealized rectangular forms to represent sastrugi. These models can explain some of the observed effects of sastrugi on bidirectional reflectance, but they tend to exaggerate those effects, probably because of the idealized shapes used in the models. Some of their results are discussed in section 5.4 below.

4. Measurements at South Pole Station

4.1. Experimental Design

A satellite pixel of a sastrugied snow surface will always contain many sastrugi. For near-surface measurements to be applicable to interpretation of satellite measurements, it is therefore important to view a "footprint" of surface area sufficiently large to contain a representative distribution of sastrugi slopes, and yet to restrict the angular field of view sufficiently to resolve the variation of R with angle. These two requirements mean that the measurements must be made from an elevated platform, which at South Pole Station is available as a 22-m walk-up tower. An advantage of the polar location is the unique condition that the solar zenith angle is nearly constant during the course of a day. The zenith angle of incidence on the ice sheet surface is also constant, because the large-scale surface slope is only 0.001. We therefore were able to sample the full range of solar azimuths relative to the sastrugi orientation, for a particular sastrugi geometry and solar zenith angle. The R pattern changes over the course of the day as the solar azimuth changes relative to the sastrugi axis. Measurements were made with 15° field of view at 15° intervals in viewing zenith and azimuth, at intervals of 1 hour (15° of solar azimuth). By making measurements throughout the sunlit season, a range of solar zenith angles from 67° to 90° was sampled.

We were unable to investigate the effect of snow grain size on R because the average grain size of surface snow does not vary much from day to day or month to month on the Antarctic Plateau, since the surface is continually renewed by small amounts of precipitation nearly every day, and there is never any melting. The grain sizes were frequently photographed; mean radii at the surface were almost always in the range 50-70 μm, increasing to 100-200 μm at 10-cm depth. Some of these photographs were published by *Grenfell et al.* [1994].

The tower is located at the edge of the Clean Air Sector, which is usually upwind of the station buildings. From the top of the tower, a continuous sweep of about 210° of azimuth contains undisturbed snow of the Antarctic Plateau;

the other 150° contains buildings and footpaths. A manually operated goniometer (angle-setting device) was attached to an arm extending 0.5 m from one corner of the tower, parallel to one side. A radiance probe with a circular field of view of 7.5° radius (15° full width) was mounted on the goniometer, and attached to the spectral radiometer by a fiber optic as shown in Figure 2. The radiance probe was constructed of black anodized aluminum with three internal baffles to minimize internal reflections. A bubble level on the goniometer was used to align a viewing zenith angle of 90° with the horizon. Azimuthal alignment of the goniometer was achieved by observing the shadows of the tower and the probe. The orientation of one side of the tower was determined to be parallel to longitude 033°E by noting the clock time when the shadows of two adjacent legs of the tower overlapped, together with the equation of time for that date. A similar analysis was done with the probe to verify that it was oriented parallel to the plane of the two tower legs when the goniometer azimuth read 0°. The procedure was repeatable to ±0.5°. The goniometer was lubricated with low-temperature silicone grease and operated well in summer, but the grease proved to be too viscous below -40°C. During the winter of 1992 the grease was replaced with graphite powder for cold-weather operation, which performed well down to the coldest measurement conditions (-65°C).

The radiance probe was attached to a small spectral radiometer designed and built by Peter Mullen [*Grenfell et al.*, 1994]. In normal use this instrument has a rotating wheel containing 11 interference filters of 10-nm bandwidth. For this study we used a limited set of wavelengths: 600 or 660 nm to represent the visible, and 900 nm in the near-infrared where atmospheric Rayleigh scattering would be negligible. The spectral transmission of these filters was measured before and after the field seasons; their bandwidths and peak wavelengths remained unchanged. Radiometric calibration of the radiometer was not necessary because our analysis procedure requires only relative measurements of radiance.

Grounding wires were attached to the radiometer, data logger, and human operator to discharge static electricity. The instrument's detector was a silicon photodiode connected to an operational amplifier with four amplification levels and controlled by a Polycorder 516B data logger to measure relative radiance. At the beginning and end of each scan, the radiance probe was covered and the voltage corresponding to the dark current was recorded. The average of this voltage was later subtracted from the signal. The dark current was minimized by adjusting the current offset of the operational amplifier. The radiometer and data logger were housed in an insulated box and maintained at about 10°C by an electric heater. After several sets of hourly measurements were completed, the data logger was removed from the box, brought to the Clean Air Facility, and downloaded to a computer.

Measurements of relative radiance were made at 14 azimuth positions from -90° to +105° (relative to the azimuth of the side of the tower) in 15° increments, and at five nadir angles: 22.5°, 37.5°, 52.5°, 67.5°, 82.5°. Because the probe's field of view is 15°, these measurements collected radiation from the range of nadir angles 15°-30°, 30°-45°, 45°-60°, 60°-75°, and 75°-90°, respectively. A complete set of 70 measurements usually took 10 min, but in March 1992 before the lubricant was changed, several scans at low solar elevation took up to 30 min due both to low temperatures, which made the goniometer difficult to operate, and to low radiance levels, which required extra time for the amplifier to stabilize.

Because our instrument was located at the top of a tower, we did not look at a particular patch of snow from a variety of angles, as was done in many of the experiments cited above. Instead, in our experiment each "footprint" sampled is at a different location on the snow surface. We therefore require that the snow surface have uniform albedo and be statistically uniform in its roughness characteristics within each footprint. These conditions are satisfied for measurements at the larger viewing zenith angles, but for the view closest to nadir (θ_r=22.5°) the footprint was too small to contain a representative sample of sastrugi, with consequences that are discussed below.

For each scan the sky conditions were noted, and scans were used in our analysis only for times when there was a clear sky, or a very small amount of cloud near the horizon in a region of the sky far from the Sun. Visual observations alone could not be trusted to detect a very thin veil of cloud in front of the Sun, so additional confirmation of clear sky was required. We made use of instruments on the roof of the Clean Air Facility, 90 m from the tower, operated by the Climate Monitoring and Diagnostics Laboratory of the National Oceanic and Atmospheric Administration (NOAA-CMDL). Measurements from a four-wavelength normal-incidence pyrheliometer, and from a filtered pyranometer measuring near-infrared flux, were recorded every 3 min. Usually at least one of these instruments was in operation and proved valuable for selection of hours for which the solar beam was constant during the 10-30 min required to carry out the angular scan.

If the sky remained clear and personnel were available, the full set of measurements was ideally repeated at hourly intervals, as the Sun moved around 15° in azimuth every hour. Usually, however, changing sky conditions meant that several days were required to obtain a complete set of measurements at each of the 24 solar azimuths.

4.2. Generation of Anisotropic Reflectance Patterns

During the course of a day at the South Pole, the solar azimuth ϕ_o (relative to the Greenwich Meridian) advances 15° per hour while the sastrugi orientation remains fixed relative to the lines of longitude. However, R patterns are usually presented with the solar direction defining the zero of azimuth, and we follow that convention here. We therefore define the relative viewing azimuth $\phi \equiv \phi_r - \phi_o$, and use the symbol ϕ_{sas} to mean the angle between Sun and sastrugi (Figure 1), so ϕ_{sas} varies from 0° to 360° over the course of a day.

Because the Sun is always low at the South Pole, in the discussion below we often find it more convenient to identify R patterns by their solar elevation angle h rather than their zenith angle θ_o, where θ_o=90°-h.

Each of our scans collected data for slightly more than half of an R pattern, limited to an azimuth range of 195°, but by overlapping one scan with another taken 12 hours later, it is possible to create a complete R pattern at all azimuths for the particular ϕ_{sas}. This procedure assumes that $R(\phi_{sas}) = R(180° + \phi_{sas})$, i.e., that the longitudinal orientation of sastrugi can affect R but that R is unaffected by interchanging the windward (nose) and leeward (tail) ends of sastrugi. We have

given the name "stitching" to the process of combining two half-patterns to obtain a complete R pattern, which involves application of a scale factor to one of the two half-patterns. Scaling is necessary because over the 4-7 days that were often needed to acquire a complete set of 24 scans under clear sky, the downward solar flux changed slightly as the solar declination slowly changed, and the instrument's response function may also have drifted.

When two corresponding half-patterns are merged, they overlap in two 15° wedges, with radiance measurements in common at 20 angles. These overlapping wedges are used to stitch the two complementary half-patterns together. The overlapping values from one half-pattern are divided by those of the other, creating 20 scale factors. At a particular viewing nadir angle θ_r in each of the two wedges there is a pair of scale factors on adjacent azimuths (the right and left boundaries of each wedge), a total of 10 pairs of scale factors. One member of each of these pairs is now rejected, and the other chosen, so as to minimize the variation among the ten chosen scale factors. The reason for choosing just one scale factor from each pair is that sometimes the shadow of the tower, or even the shadow of the Clean Air Facility when the Sun was very low, impinged on one of the adjacent positions. The ten selected scale factors are then averaged to obtain a single scale factor, which is used to scale the second half-pattern to the first. No systematic pattern was found among the ten scale factors that would indicate a difference in the R patterns 12 hours apart; this supports our assumption that R is unaffected by interchanging sastrugi noses and tails.

Next the shadow of the tower is identified in the pattern; it affects several of the radiance measurements in the backscattering direction. Each measurement affected by the shadow is discarded, and in its place is inserted the average of the two neighboring measurements at the same nadir angle.

After a pair of half-patterns is stitched together, all values in the complete plot are divided by the average radiance, in the manner described by *Taylor and Stowe* [1984a,b], to yield the anisotropic reflectance function R:

$$R(\theta_r,\phi)=\frac{\pi L(\theta_r,\phi)}{\int_0^{2\pi}\int_0^{\pi/2} L(\theta_r,\phi)\cos\theta_r \sin\theta_r \, d\theta_r \, d\phi}, \quad (4)$$

where L is the measured radiance. The resulting R function has an average value of 1.0 over the (θ_r,ϕ) hemisphere, as required. One advantage of measuring a complete angular pattern and then normalizing it to obtain R is that our instrument does not need to be calibrated with a diffuser plate that approximates a Lambertian reflector, which may be needed if only a limited range of angles is measured, and as was done, for example, by *Carlson and Arakelian* [1993]. Calibration by means of a diffuser plate requires knowledge of the spectral dependence of the diffuser plate's reflectivity and the deviations of its reflectance from Lambertian, and requires that the diffuser plate be oriented parallel to the large-scale snow surface, all of which lead to uncertainty in the values obtained for R.

To convert a value of R into a value of the bidirectional reflectance ρ via (2), it is necessary to know the albedo A_s. The albedo was measured in a separate experiment [*Grenfell et al.*, 1994]; across the visible and near-ultraviolet the albedo is insensitive to grain size and zenith angle and nearly constant at a value of 0.96-0.98.

Table 1 lists all of our measurement series during three different years at South Pole Station. Cloudy periods limited our ability to acquire complete sets of 12 matched pairs (ϕ_{sas} from 0° to 180°), especially at low solar elevations.

5. Experimental Results

Before showing the effect of sastrugi orientation, we first present just the daily average of the anisotropic reflectance pattern; i.e., the average of the individual R patterns for 12 different values of ϕ_{sas}. To further reduce noise due to sastrugi, the two halves of the plot (on opposite sides of the principal plane containing the Sun and the surface normal) are averaged. We use *Taylor and Stowe's* [1984a,b] method of

Table 1. List of Experiments at South Pole Station

Date	Solar Elevation, deg	Wavelength, nm	Number of Scans	Number of Matched Pairs	Comments
1986					
February 7-12[a]	15.0	900	26	7	
1991					
January 2-8[b]	22.7	900	31	12	complete set
January 28-31	18.0	660	27	12*	complete set
February 3-4	16.5	900	18	6	
1992					
February 17-24	10.4	600	17	4*	
March 2-4	6.8	600	16	6*	
March 6-7	5.2	600	3	1	changing sky
March 9-14	3.5	600	16	2*	
March 17-19	0.7	600	3	1*	
October 5-6	4.9	600	6	1	changing sky
October 14-20	9.4	600	28	11	changing sky
October 27-30	13.3	600	25	12*	complete set
December 8-11	22.9	600	25	12*	complete set
December 14-22	23.3	900	20	8	

*Data from these experiments were used to develop the parameterization, with measurements at wavelength 600 or 660 nm and stable clear-sky conditions during individual scans.
[a]Some of these results were shown in Figure 13 of *Grenfell et al.* [1994].
[b]Some of these results were shown in Figure 1 of *Brandt et al.* [1991].

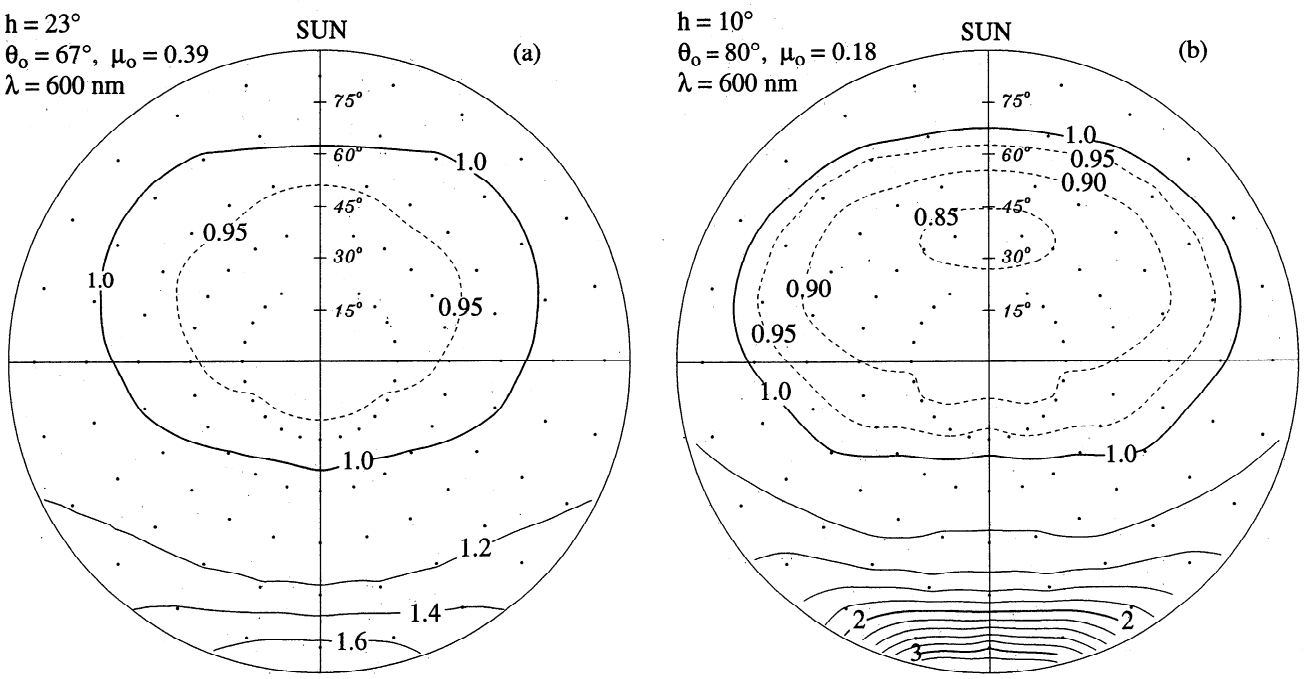

Figure 3. Effect of solar elevation on anisotropic reflectance factor of snow. Measurements of R from the 22-m tower at South Pole Station, averaged over all Sun-sastrugi azimuths ϕ_{sas}, i.e., "daily" average, at wavelength 600 nm and at two solar elevation angles h: (a) h=23°; (b) h=10°. Points indicate viewing angles where measurements were taken, at 15° intervals in viewing zenith and azimuth. Solid contours for R >1, with intervals 0.2; dashed contours for R<1, with intervals 0.05.

displaying R. On these plots the radial coordinate is proportional to the viewing zenith angle θ_r, and the azimuth ϕ between the Sun and the detector is represented by the azimuthal coordinate. The Sun is located at the top of each plot, so the bottom of the plot is the forward-scattering direction.

5.1. Variation of R With Solar Elevation Angle

For the range of solar elevations experienced at the South Pole (0°-23.5°), the most nearly isotropic pattern obtained was that at the highest solar elevation (Figure 3a). The most anisotropic pattern, with the strongest forward peak, was obtained not near h=0° but rather at h=10° (Figure 3b); the reason for this is explained below. The forward peak at h=10° is 3 times the average brightness; at h=23° is it only 1.6 times. There are two contour intervals in these plots: solid contour lines in steps of 0.2 for values of R>1, and dashed contours at steps of 0.05 for R<1 to show detail in the plot's center where the variation of R with angle is much less. Points marked on the plots indicate the angles at which measurements were made. These plots are typical of our snow reflectance patterns averaged over ϕ_{sas} ("daily averages"), with a forward peak usually at least twice as bright as the average of the scene, and a minimum of R located 20°-40° backward of the nadir direction. These two examples will be used again in section 6 below to illustrate the parameterization of R.

During February and March 1992, our measurements may have been affected by volcanic aerosol from the Pinatubo volcano, which diffused the solar beam somewhat. However, the scattering by these aerosol particles was mostly into the near-forward direction, so because of our 15° angular field of view we would not expect to see its effect in our R patterns. In a comparison of R patterns at the same θ_o in autumn and spring of 1992, no effect of this aerosol was detected. We therefore think that our results apply to all "clear-sky" conditions, whether or not they contain volcanic aerosol.

5.2. Variation of R With Wavelength

Figure 4 displays two daily-average R patterns for nearly the same solar elevation (h≈17°) but different wavelengths, 660 and 900 nm. The two patterns are very similar, in agreement with the lack of dependence of BRDF on wavelength across this spectral region found by *Griggs and Marggraf* [1967], even though the albedos are somewhat different (A_s =0.96 at 660 nm and A_s =0.88 at 900 nm [*Grenfell et al.*, 1994, Figure 4]). Based on considerations discussed in section 3.4 above, we think it likely that for clean fine-grained snow the R pattern is independent of wavelength from 300 to 700 nm, because ice absorption is very weak across this entire spectral domain and the albedo is uniformly high (A_s≥0.96). However, measurements such as we made from the tower would not be able to show this. Our method is capable of measuring R only at wavelengths greater than about 600 nm where the incident radiation under clear sky is a direct beam from the Sun, with little sky brightness due to Rayleigh scattering. (The bidirectional reflectance is defined as the scattering pattern for an incident direct beam from a single direction.) At shorter wavelengths what would be measured is not the R pattern for incidence from (θ_o,ϕ_o) but rather a weighted average of R patterns for the direct and diffuse components of the incident radiation. Thus the pattern of radiation reflected from a snow surface under a clear sky is more isotropic at 300 nm than at 700 nm even

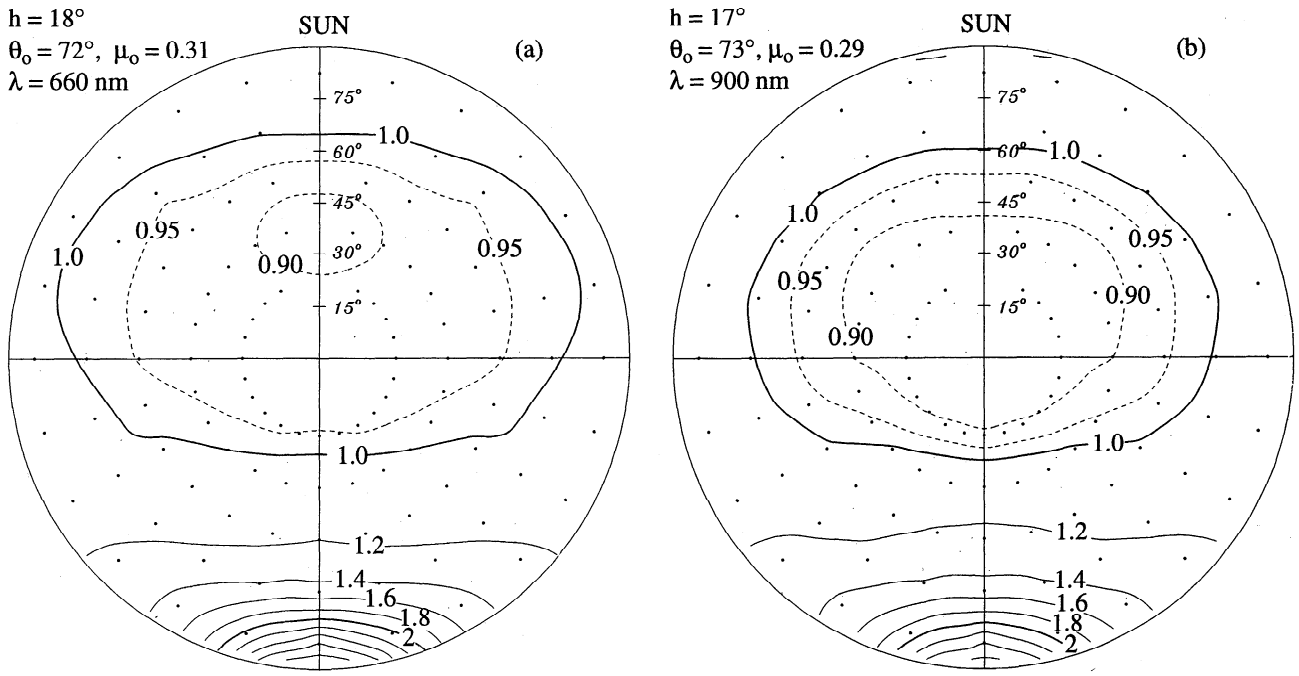

Figure 4. Wavelength dependence of R. Daily averaged anisotropic reflectance factor at a solar elevation of 17-18°, at wavelengths of (a) 660 nm and (b) 900 nm. Contour increments are the same as those used in Figure 3.

though R is the same at both wavelengths, because of the different distributions of downward incident radiance.

Based on these considerations, and on the similarity of Figures 4a and 4b, we think the results of our experiments (and the parameterization below for 600 nm) can be used for the entire wavelength range 300-900 nm, but not at longer wavelengths in the near-infrared, where snow becomes more absorptive. However, even at 600 nm, the diffuse fraction becomes significant at very low Sun, as will be shown below, so the generality of our results to other wavelengths strictly applies only for solar elevations greater than about 10°.

5.3. Variation of R With Sastrugi Azimuth

In Figure 5 are displayed four individual hourly R patterns selected from the complete set of 12 patterns at λ=900 nm obtained on January 2-7, 1991 [*Brandt et al.*, 1991]. The sastrugi in January-February 1991 were mostly aligned along the 10°E longitude direction but they were small, averaging 20-cm height (peak to trough); measurements for seven individual sastrugi are given in Table 2. However, even though the sastrugi were small and the Sun was high (just past solstice, h=23°), the patterns at different times of the day are notably different. At 0530 UT, when the solar azimuth was perpendicular to the sastrugi (ϕ_{sas}=90°), the forward peak was only 2.0 times the mean brightness; it increased to 2.8 times the mean brightness when the Sun was parallel to the sastrugi (ϕ_{sas}=0°) at 1130 UT. In the perpendicular case the Sun-facing sides of sastrugi enhance the normally smaller backscattering peak, while the side facing away from the Sun is shaded so the forward-scattering peak is diminished. When the solar azimuth is at an intermediate angle, as shown in Figure 5 for 0330 UT and 0730 UT, the reflection pattern becomes asymmetric about the principal plane. Such asymmetry was also observed by *Kuhn and Siogas* [1978].

An important message from Figure 5 is that the variation of ϕ_{sas} causes R to change greatly at large viewing angles θ_r, but the near-nadir part of the pattern (θ_r<50°) is not much affected. In other words, as the Sun moves around in azimuth to become perpendicular to the sastrugi, the forward peak weakens, but the photons lost from the forward peak do not show up in the nadir direction; they are redirected mostly in ϕ rather than in θ_r. A subtraction of the 1130 pattern from the 0530 pattern of Figure 5 shows a trade-off between forward and backward hemispheres, predominantly at large viewing angles, θ_r>60°, but the azimuthal average of the inner ring at θ_r =22.5° increases by only ΔR=0.02. Model calculations actually show a slight reduction of the nadir intensity for ϕ_{sas}=90° compared to ϕ_{sas}=0°, which is not seen in the observations and probably results from the idealized rectangular geometry of the model's sastrugi [*O'Rawe*, 1991, Figures 6.11f and 6.11i; *Leroux and Fily*, this issue, Figures 8 and 9].

To quantify the sensitivity of R to ϕ_{sas}, the 12 individual patterns at ϕ_{sas}=0°, 15°, 30°, . . . , 165° are each subtracted from the mean of these 12 patterns, and the root-mean-square (rms) difference δ is plotted (in percent) in Figure 6. This rms difference is shown for the two cases whose averages over ϕ_{sas} were shown in Figure 3, with solar elevations h=23° and h=10°. The sensitivity of R to ϕ_{sas} is smaller at high Sun (Figure 6a) for all viewing angles. The rms difference is greatest in the forward peak, δ =11% for h=23° and 20% for h=10°.

Proceeding inward from the perimeter of Figure 6, δ decreases to about 4% at a viewing angle θ_r =52.5° for h=23° and 5% for h=10°. We expect the decrease of δ to continue as θ_r decreases toward nadir viewing. A mild decrease is seen in Figure 6a (h=23°), but not in Figure 6b (h=10°), where δ actually increases to 6-9% for near-nadir viewing. This large variability at θ_r =22.5° is almost certainly an artifact due to the small footprint at that viewing angle, which consists of only a few sastrugi and therefore often contains an unrepresentative distribution of shaded and sunlit faces. The measurements at larger θ_r have much larger footprints, approximately proportional to $(1+\tan^2\theta_r)$. We think that measurements made

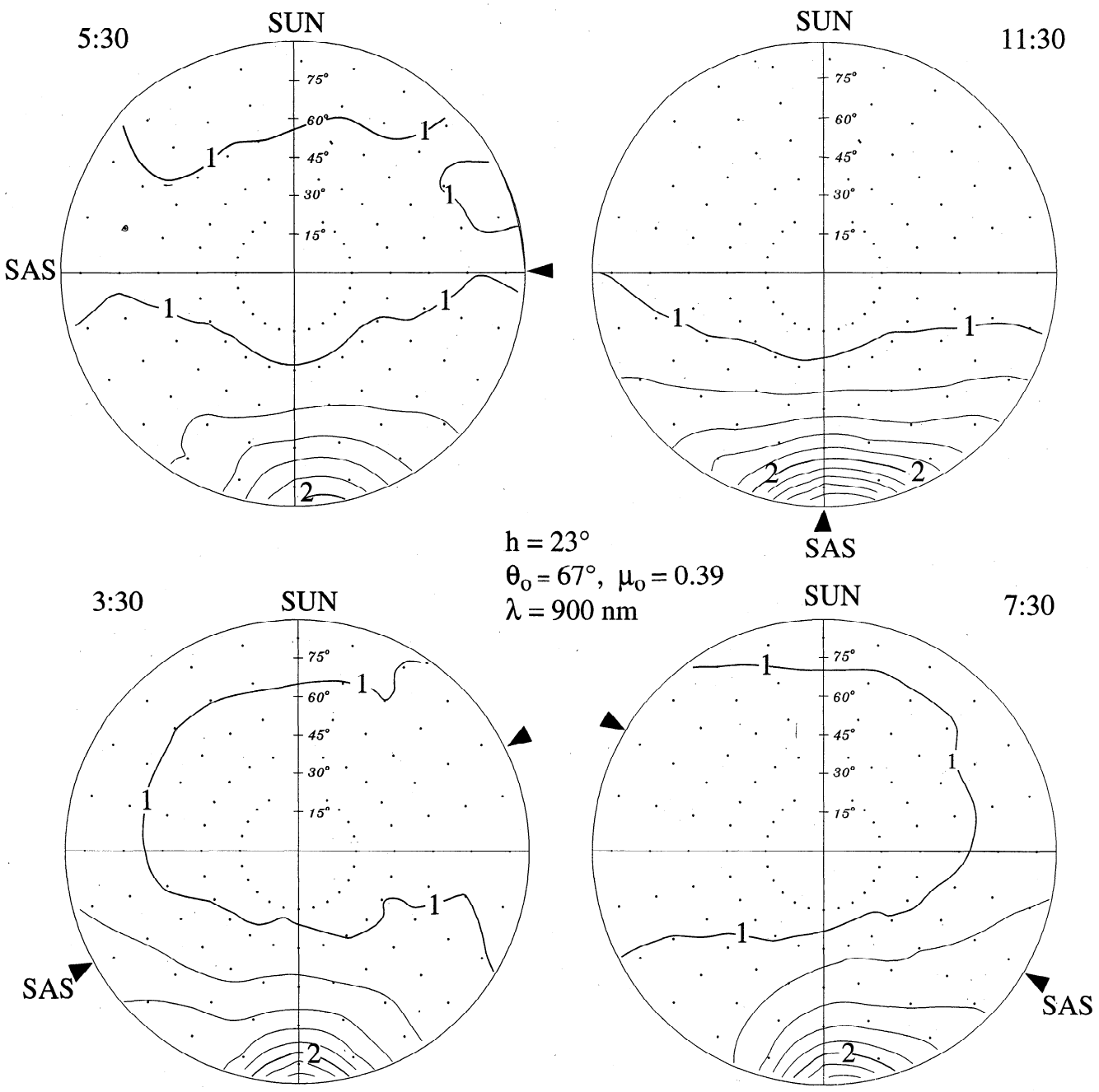

Figure 5. Anisotropic reflectance factor for h=23°, λ=900 nm, for four different Sun-sastrugi azimuth angles. The orientation of the sastrugi axis is indicated by SAS. The universal time of each pattern is indicated. Adapted from Figure 1 of *Brandt et al.* [1991].

from a much higher tower would show δ decreasing to a minimum at nadir.

In an analysis of visible-channel data from polar-orbiting satellites, which is not subject to this sampling error we have from the tower, *Doherty* [1997] found the day-to-day variability, geographical variability, and interannual variability of R over the East Antarctic Plateau (after accounting for variable ozone absorption) all to be smallest at near-nadir viewing angles, in agreement with our expectation.

Table 2. Dimensions of Seven Sastrugi at South Pole, February 1991 (Typical of Summertime Sastrugi).

Feature	Height, m	Length, m	Width, m	Height-to-Width Ratio
1	0.25	15.0	4.0	0.06
2	0.20	5.4	1.8	0.11
3	0.10	8.0	1.2	0.08
4	0.25	4.0	2.0	0.12
5	0.23	2.2	1.3	0.17
6	0.09	1.1	0.9	0.10
7	0.24	6.5	0.7	0.34

5.4. Comparison of Measurements to Models of Sastrugi Reflectance

Leroux and Fily [this issue] have attempted to explain the set of four patterns shown in Figure 5, using a radiative transfer model for snow in which the sastrugi are modeled as rectangular box-like protrusions. Their model was successful in obtaining the qualitative differences of these four patterns but obtained forward and backward peaks larger than

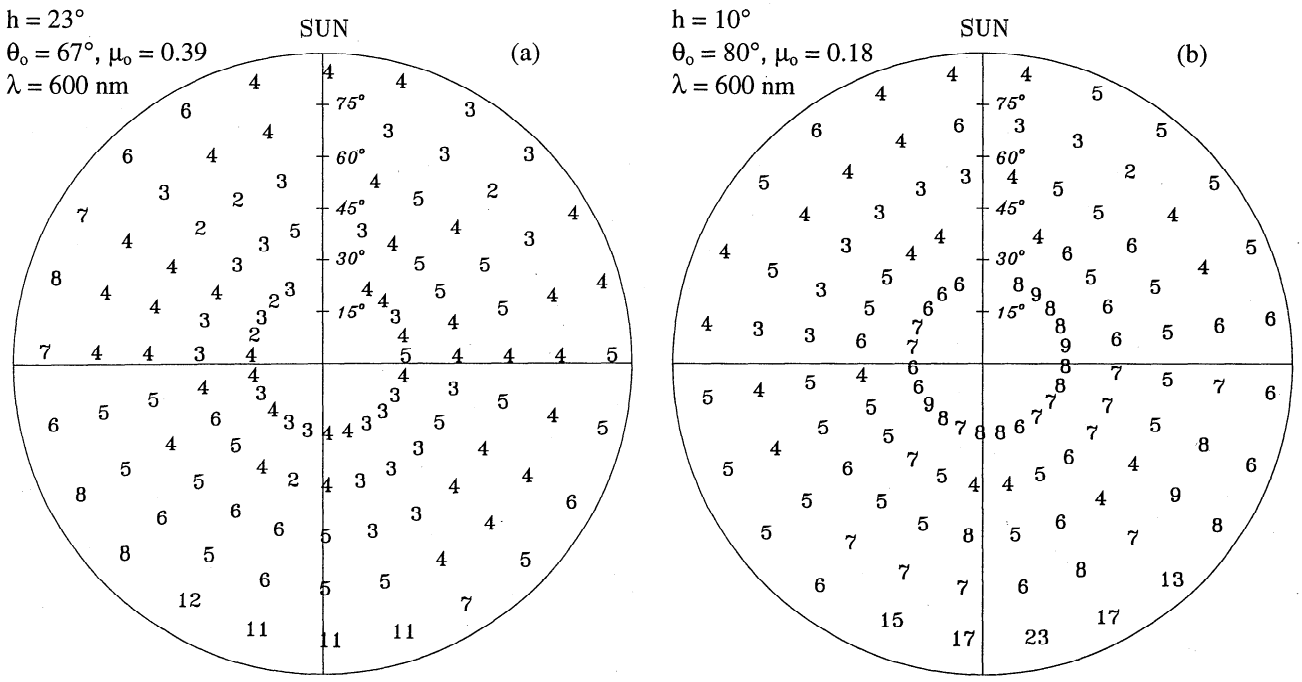

Figure 6. Variation of R due to sastrugi orientation. The hourly values of R at each viewing angle (θ_r, ϕ) are compared to the daily mean shown in Figure 3. The root-mean-square (rms) difference of the 12 values at each point is plotted here in percent: (a) h=23°, (b) h=10°. The large rms errors in Figure 6b at near-nadir viewing (6-9% at θ_r=22.5°) are biased high due to inadequate footprint size, as discussed in section 5.3.

observed, probably because the model sastrugi were all perfectly parallel and had vertical walls, whereas the real sastrugi in our experiments had a distribution of orientations ϕ_{sas} and often had gently sloping sides rather than vertical walls (Figure 7).

O'Rawe [1991] used a Monte-Carlo radiative transfer model to compute the reflectance patterns from sastrugied snow, assuming either a pure direct beam or pure diffuse incidence, and assuming R patterns for flat snow to be those given by *Taylor and Stowe* [1984b]. She computed R patterns for sastrugi with several values of flat-surface albedo (corresponding to different wavelengths), solar zenith angle, and solar-sastrugi azimuth angle. Height-to-width (h/w) ratios of 1.0, 0.5, 0.2, 0.1, 0.05, and 0.01 were used, and the sastrugi width was set equal to the sastrugi spacing (Figure 7). Her calculations are not available for θ_o=67°, but we can compare our Figure 5 to her results for θ_o=60°. The left-right asymmetry for ϕ_{sas}=60° at 0330 and 0730 is best matched in her model results for h/w=0.05, whereas the observed sastrugi had h/w≈0.1 (Table 2). As in Leroux and Fily's model, O'Rawe's model produces an exaggerated backscattering peak for perpendicular sastrugi (ϕ_{sas}=90°) that exceeds the forward peak for all values of h/w≥0.05, whereas in our observations (Figure 5, at 0530) the forward peak is always larger.

5.5. Forward Peak and Near-Nadir Views

Figure 8 shows the value of R in the forward peak (θ_r=82.5°, ϕ=180°) for each daily averaged R pattern, plotted versus solar elevation angle h. As h decreases from 23° to 10°, the forward peak increases but then decreases as the Sun continues to approach the horizon. This decrease is due to the increasing fraction of diffuse radiation from the sky, relative to the direct beam, as the Sun approaches the horizon. For h<10° we only have measurements at λ=600 nm. If measurements were made at longer wavelengths in the near-infrared, the illumination would be essentially a direct beam down to lower solar elevations, and we would expect the forward peak of R to continue to increase.

The outlier in Figure 8, with R=4.3 at h=15°, comes from the R pattern measured in February 1986 that was shown as a

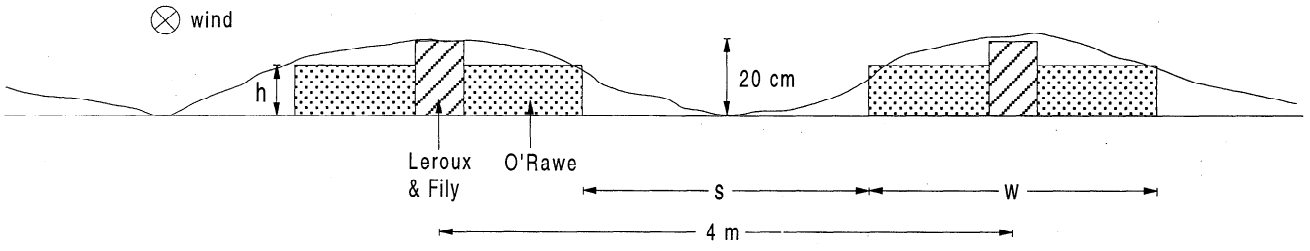

Figure 7. Cross sections of sastrugi used in the models of *O'Rawe* [1991] and *Leroux and Fily* [this issue], compared to typical shape of natural sastrugi on the Antarctic Plateau. View is parallel to the wind direction. The height, width, and spacing of sastrugi in O'Rawe's model are indicated by h, w, and s.

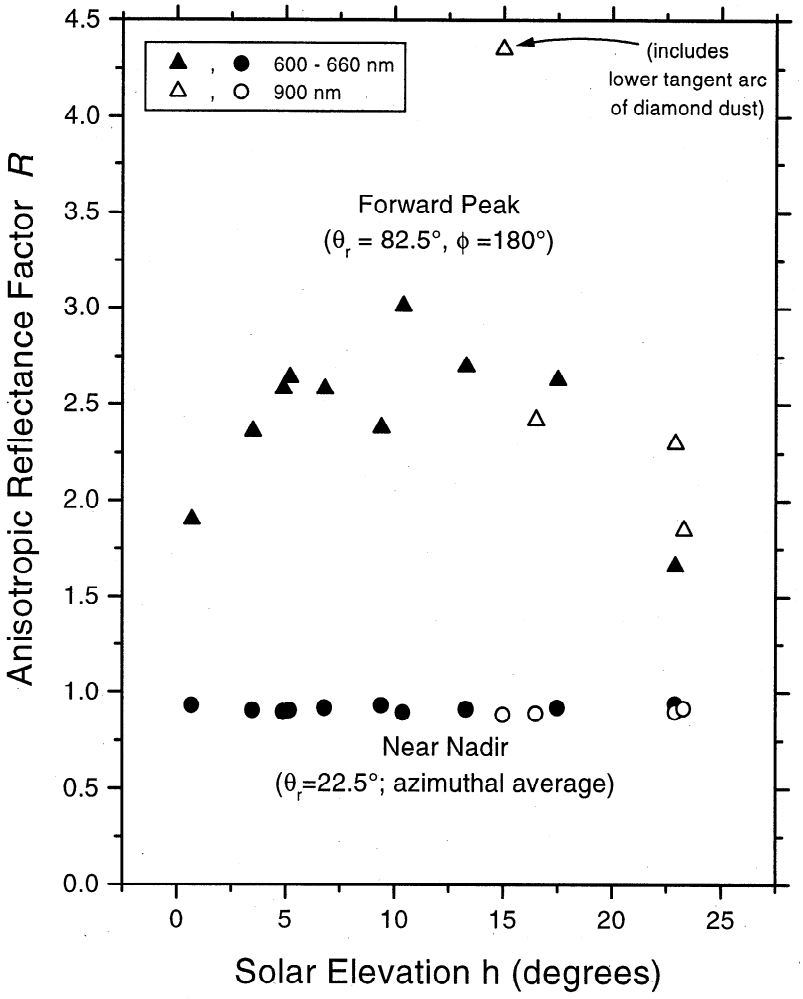

Figure 8. Anisotropic reflectance factor of the forward peak (θ_r=82.5°, ϕ=180°; triangles) and the near-nadir view (θ_r=22.5°, azimuthal average; circles) for each of the measurement periods listed in Table 1, plotted as a function of solar elevation. Each point is the daily average, i.e., the average over all available sastrugi azimuths ϕ_{sas}. Near-nadir values are further averaged over all viewing azimuths ϕ to compensate for the limited footprint when the sastrugi field is viewed vertically, as discussed in section 5.3. The outlier at R=4.3 is affected by atmospheric halos due to ice crystals in the lowest 22 m of the atmosphere, between the snow surface and the instrument, as discussed in section 5.5.

daily average in Figure 13 of *Grenfell et al.* [1994]. We now have an explanation for the unusual strength of this bright spot. Most of the radiance scans that contributed to that average R pattern were made under conditions of clear-sky ice-crystal precipitation, or "diamond-dust." These small ice crystals form in the near-surface air as humid warmer air is mixed down from the top of a surface-based temperature inversion, forming an optically thin "mixing cloud" [*Bohren*, 1987] that is responsible for the frequently observed halos. The 22° halo was prominent around the Sun during the BRDF measurements in February 1986. Although we lack detailed notes of halos for those days, based on our experience of observing halo complexes at the South Pole it is likely that a lower tangent arc [*Tape*, 1994] was also present, forming a very bright spot at the bottom of the 22° halo, which would have been located 7° below the horizon because the solar elevation was 15°. When measuring the forward peak at θ_r=82.5°, our radiance probe was thus aimed directly at this lower tangent arc, and the enhanced brightness in this direction was due to scattering by well-formed horizontally oriented hexagonal columns in the atmosphere below 22-m height. The snow surface itself also can occasionally exhibit halos but normally does not because after falling to the surface, the snow crystals soon lose their sharp edges and flat faces due to vapor transport [*LaChapelle*, 1969].

If we ignore the outlier, the forward peak does not exceed 3.0 at any solar elevation. When a flat surface is roughened, the forward peak is reduced because bumps cause shading on their sides opposite the Sun. Natural surfaces with randomly oriented roughness therefore exhibit a weaker forward peak than do model calculations for a flat surface [*McKee and Cox*, 1976]. Radiative transfer models for the bidirectional reflectance of flat snow exhibit a strong forward peak at visible wavelengths. *Li* [1982, Figure 9] reported R=3.9 for θ_o=74°; *Leroux and Fily* [this issue, Figure 7] reported R between 4 and 5 for θ_o=67°, with perhaps an average of R=4 over a 15° field of view; and *Han et al.* [1998, Figure 1a] found R greatly exceeding 3 (contour lines cease to be drawn for θ_r>72°) for θ_o=70°. By comparison, for the sastrugied surfaces in Figure 8 the measured forward peak at θ_o=67° is much lower, R≈2.0±0.3. This difference between model and observation is also found for clouds. *Stuhlmann et al.* [1985]

used a radiative transfer model to derive a spectrally averaged R for a horizontally homogeneous cloud and showed that it exhibited a stronger forward peak ($R\approx4.0$ at $\theta_o=72.5^o$) compared to the average forward peak of $R\approx2.4$ obtained at this solar zenith angle from satellite observations [*Taylor and Stowe*, 1984a,b] for all middle-level clouds, many of which had bumpy tops.

Also shown in the lower part of Figure 8 are the azimuthal averages of the near-nadir ($\theta_r=22.5^o$) values of R; they are nearly independent of solar elevation. To summarize this figure and the earlier figures, it is apparent that by comparison to any other viewing directions, the near-nadir R is relatively insensitive to solar elevation, viewing azimuth, and sastrugi orientation. Our recommendation will be that if a satellite measurement at visible or ultraviolet wavelengths is to be used to infer snow albedo, or used for remote sensing over snow of atmospheric properties such as ozone amount, where the surface bidirectional reflectance must be known as a lower boundary condition, then it is best to use near-nadir views.

This conclusion is opposite that of *Davies* [1984] for the case of broken clouds over a dark surface. He found that the albedo of a scene was most accurately inferred from an oblique view, $\theta_r\approx60^o$. The R function of patchy clouds differed greatly from that of horizontally extensive clouds in near-nadir views, but differed little at $\theta_r=60^o$ because at oblique viewing the field of view is filled with cloud, even in the case of patchy clouds, since the sides of clouds hide the underlying surface. Davies's result favoring an oblique view would probably apply as well to clouds (over dark surfaces) that are continuous but of variable optical thickness, or continuous but with bumpy tops. The reason that for snow a nadir view is safe, and even preferred, is probably that snow, unlike clouds, is optically thick and usually semi-infinite. For clouds over snow, the albedo and bidirectional reflectance are similar to those of cloud-free snow [*Han et al.*, 1998], and the variability of R is again probably smallest near nadir [*Doherty*, 1997].

On the other hand, if the effects of sastrugi are to be exploited rather than avoided, for example, to use sastrugi orientation to infer wind direction, then oblique views are preferred over near-nadir views. However, inference of sastrugi orientations from satellite may be difficult because it would probably require views at several different satellite azimuths ϕ at the same ϕ_{sas}, which could only be obtained from multiple satellites.

6. Parameterization

The measured R patterns can be fitted by simple analytical functions which will yield a value of R for any combination of angles (θ_o, θ_r, ϕ) within the range measured, not just at the measured angles. The parameterization is developed using the seven measurement periods during 1991 and 1992 that were made at 600-660 nm wavelength and met our criteria for steady solar flux and clear sky. These measurements are labeled with asterisks in Table 1. For remote sensing, an a priori knowledge of the distribution of sastrugi dimensions and orientations for a particular time and location in Antarctica is difficult or impossible to obtain, but in Figure 6 we showed that if the viewing zenith angle is limited to $\theta_r\le50^o$, variation in R due to sastrugi orientation is at most 7-8%. We therefore have chosen to limit our parameterization to $\theta_r\le50^o$ and to ignore sastrugi azimuth, so we use the daily average patterns to develop the parameterization, in which R is expressed as a function of three angles: θ_o, θ_r, ϕ. Our parameterization is applicable for dry, fine-grained snow (radii 50-200 μm) at visible wavelengths but only within the range of solar zenith angles measured, i.e., those available at the South Pole, $67^o\le\theta_o\le90^o$.

At the largest zenith angles, 80-90°, our measurements are affected by diffuse Rayleigh-scattered light from the sky as discussed above, so the parameterization for this range of θ_o describes the measurements rather than the ideal pattern for direct-beam illumination. However, for practical satellite applications using reflected sunlight in the visible or ultraviolet at low Sun, the snow surface will never be illuminated just by a direct beam, and the diffusion of the radiation incident onto the snow surface can actually be an advantage for remote sensing, as it reduces the capability of sastrugi to influence the R pattern and also reduces the forward peak as shown in Figure 8. This means that although we recommend restricting the viewing zenith angle to $\theta_r\le50^o$ for accurate remote sensing, there is no such restriction on solar zenith angle due to sastrugi. However, large solar zenith angles are often unfavorable for other reasons, for example, the need to know the pixel-scale (1-10 km) surface slope very accurately [*Doherty*, 1997].

The azimuthal variation of R is represented by a three-term Fourier series in ϕ:

$$R(\mu_o,\mu_r,\phi)=c_1+c_2\cos(\pi-\phi)+c_3\cos[2(\pi-\phi)]. \quad (5)$$

The coefficients c_1, c_2, c_3 are functions of μ_o and μ_r as described below, where $\mu_o=\cos\theta_o$ and $\mu_r=\cos\theta_r$. Data taken at solar elevations of 10° and 23° (with maximum and minimum values of the forward peak), which were shown as contour plots in Figure 3, are now shown in Figure 9 as functions of azimuth from the forward peak (π-ϕ) for each of three viewing zenith angles 22.5°, 37.5°, and 52.5°, along with the least squares fitted three-term Fourier series (5). An alternative functional form for the variation of R with ϕ was used by *Lindsay and Rothrock* [1994] and *Knap and Reijmer* [1998], but we think the simple cosine-series is more appropriate.

To describe the dependence of R on solar zenith angle, we use a parabolic function of μ_o, as suggested by Figure 8. However, when measurements are obtained in the future for higher solar elevations (at lower-latitude Antarctic sites), it may be desirable to fit only the data for $\theta_o<80^o$, i.e., to ignore the measurements affected by Rayleigh scattering; in that case, a different functional form may be more appropriate.

To describe the dependence of R on viewing zenith angle, a linear function of μ_r proved adequate. The coefficients in equation (5) are therefore expressed as

$$c_1=a_0+a_1(1-\mu_r);$$
$$c_2=a_2(1-\mu_r);$$
$$c_3=a_3(1-\mu_r);$$

where
$$a_j=b_{oj}+b_{1j}\mu_o+b_{2j}\mu_o^2. \quad (6)$$

This functional form ensures that R is independent of ϕ when $\mu_r=1$. To define each of the four values of a_j, three values of b_{ij} are required, a total of 12 coefficients to be chosen for a best fit to the data. They are determined by a least squares fitting procedure. Daily averages of the seven datasets identified in Table 1 are used, each with a unique value of μ_o, and each containing 60 measurements of R on the 15° grid of

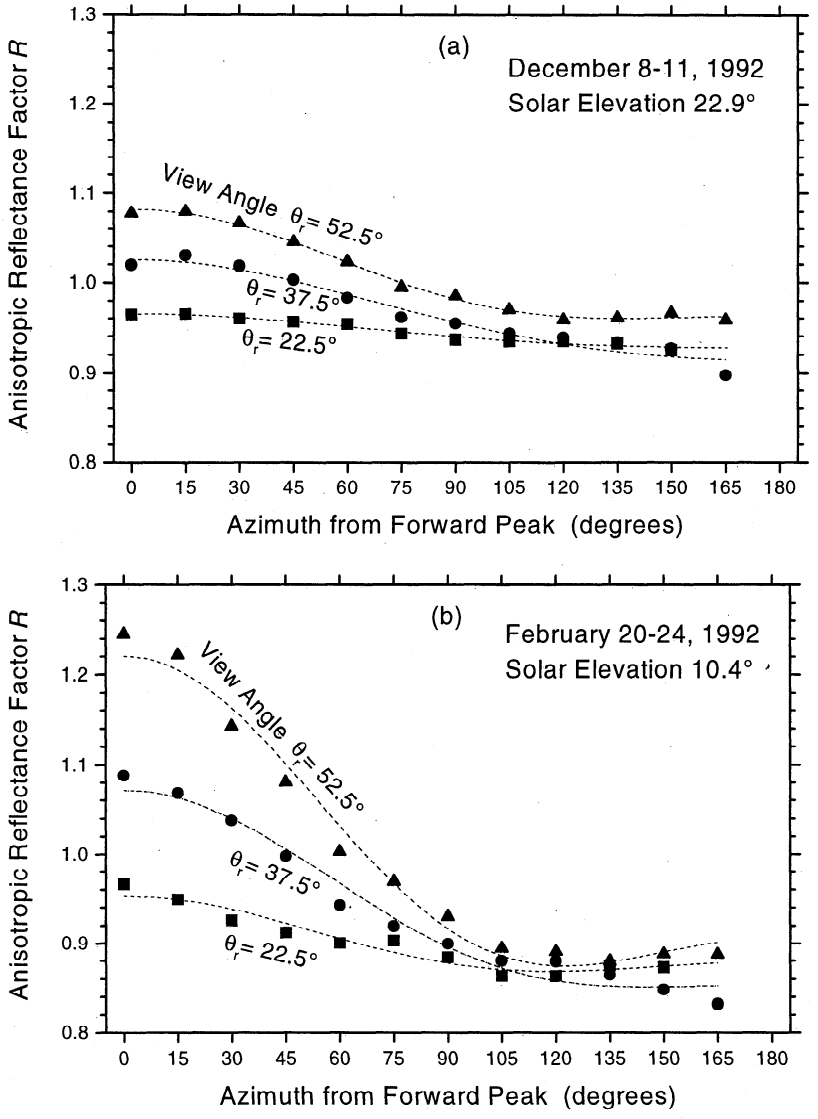

Figure 9. Anisotropic reflectance factor from Figure 3, plotted as a function of viewing azimuth relative to the forward peak (180°-ϕ), for three viewing zenith angles and two solar elevations. Least squares fits, using a three-term Fourier series, are shown as the dashed lines.

θ_r and ϕ on one side of the principal plane, giving a total of 420 measurements at different (μ_o, μ_r, ϕ) that are used to fit the 12 coefficients. The resulting values of the coefficients b_{ij} are listed in Table 3.

The parameterization of R is plotted in Figures 10a and 10b for the same two solar elevations (23° and 10°) whose measured R was shown in Figure 3. Also shown (Figures 10c and 10d) is the percent error of each of these fits. The parameterization matches the measurements to better than 5% at almost all angles, and to within 2% over a large range of ϕ, 30°-135°. The largest errors are for h=10°, where anisotropy is greatest. Figure 11 shows the rms error in percent for all seven of the measurement periods used to develop the parameterization. In general, the error of the parameterized fit is smallest at smaller viewing zenith angles or at viewing azimuths near 90°.

Table 3. Coefficients for Parameterization (Eqs. 5 and 6)

$j=0$	$j=1$	$j=2$	$j=3$
b_{00} = 0.9216	b_{01} = 0.1994	b_{02} = 0.1234	b_{03} = 0.0751
b_{10} = -0.3758	b_{11} = 0.7084	b_{12} = 2.0702	b_{13} = 0.8440
b_{20} = 1.0016	b_{21} = -1.8176	b_{22} = -4.9036	b_{23} = -2.2769

Angular range of validity: $67° \le \theta_o \le 90°$; $0° \le \theta_r \le 50°$; $0° \le \phi \le 180°$. Valid for dry, fine-grained snow (grain radii 50-200 μm) at 600-660 nm wavelength, but usable for all visible wavelengths if θ_o<80°.

7. Astronomical Applications

7.1. Dependence of R on Phase Angle

In planetary astronomy there have been many attempts to describe the reflection of sunlight by a planetary surface

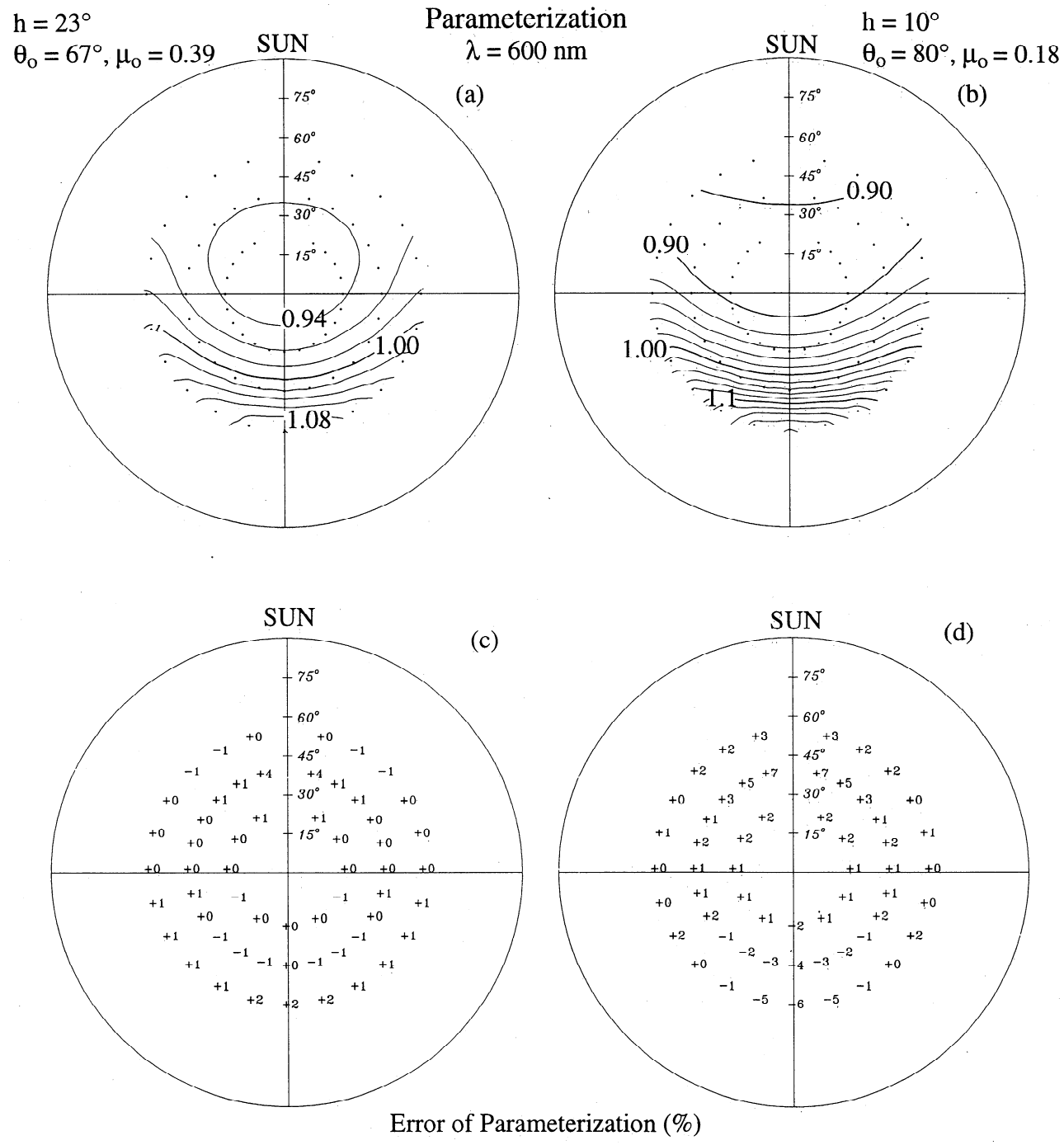

Figure 10. (a, b) Parameterization of the anisotropic reflectance factor at λ=600 nm and (c, d) percent error of the parameterization for the same cases shown in Figure 3, restricted to viewing zenith angles $\theta_r \leq 52.5^\circ$: (a, c) h=23°, (b, d) h=10°.

according to a "photometric function," in which particular functional forms for the dependence of R on θ_o, θ_r, and ϕ are assumed. The various functions that have been used were reviewed by *Hapke* [1993, chap. 8]. We have tried two of these, Minnaert's law (a function of μ_r and μ_o) and the Lommel-Seeliger law (a function of μ_r, μ_o, and phase angle α), and found that neither performs as well as a simple function of just one variable, the phase angle α. The phase angle is the angle between the detector and the source, as seen from the reflecting surface. For a planet in the solar system, viewed from Earth, α is the angle between Sun and Earth as seen from the planet. It is related to the other angles defined in Figure 1:

$$\cos\alpha = \cos\theta_o \cos\theta_r + \sin\theta_o \sin\theta_r \cos\phi. \quad (7)$$

In Minnaert's law [*Hapke*, 1981, p. 3051] the reflected intensity is proportional to $\mu_o^{\nu}\mu_r^{\nu-1}$, but the incident flux is proportional to μ_o, so R is proportional to $(\mu_o\mu_r)^{\nu-1}$, where the

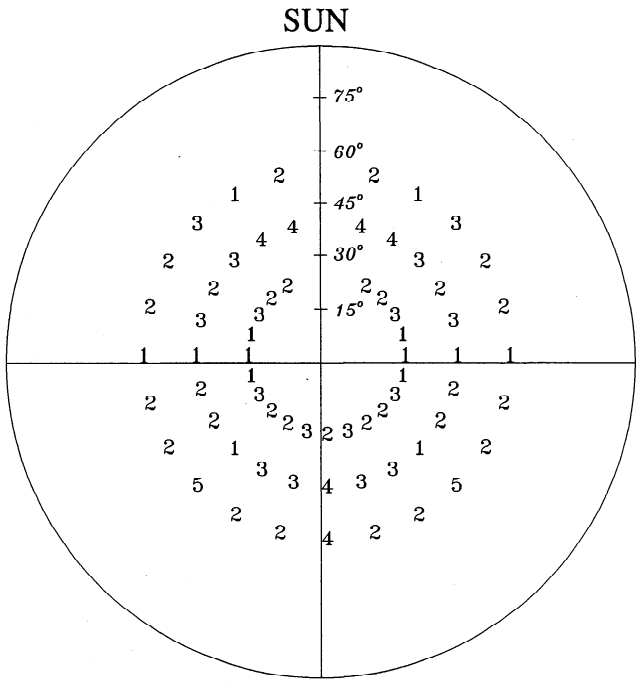

Figure 11. Root-mean-square error (percent) of the parameterization, for all seven time periods used to develop the parameterization (marked with asterisks in Table 1).

exponent is to be determined. However, when we plot log R versus log($\mu_o\mu_r$), which should give a straight line with slope ν–1, what results is not a line but rather a large spread of points for each value of $\mu_o\mu_r$. The spread is mainly due to the forward peak of R. The best fit line gives ν-1≈-0.1, implying that R is nearly independent of μ and μ_o, which, as Figures 3-5 show, is far from reality. There is no unique value of ν that can fit the data, in agreement with *Hapke's* [1993] criticism of the Minnaert function.

In the Lommel-Seeliger law, the reflected intensity is proportional to $\mu_o p(\alpha)/(\mu_o+\mu_r)$, where $p(\alpha)$ is a function to be determined, so R is proportional to $p(\alpha)/(\mu_o+\mu_r)$. We plotted $(\mu_o+\mu_r)R$ versus α but again obtained a large scatter of points rather than a single-valued function $p(\alpha)$. At particular values of α, the observed values of $(\mu_o+\mu_r)R$ were spread out over a factor-of-7 range. *Hapke* [1993, p. 200] states that the Lommel-Seeliger law is "a good description of the light scattered by low-albedo bodies . . . for which only light that has been scattered once contributes to the brightness." We therefore would not expect it to describe snow at visible wavelengths, where most of the emerging photons have been multiply scattered.

We now investigate how well R can be represented by a function of the single variable α. On Figure 12 are plotted all the values of R from the seven daily averaged patterns used to develop our parameterization above (experiments marked with asterisks in Table 1). A polynomial function might be fitted through these points and would represent the observed value of R to within ±25% for phase angles α<120°, much better than either the Minnaert law or the Lommel-Seeliger law, but much worse than our parameterization in terms of the three angles (θ_o, θ_r, ϕ).

7.2. Comments on Remote Sensing of Planetary Surfaces

Hapke [1981] presented a model for bidirectional reflectance of surfaces for planetary applications. If measurements of reflected brightness are made at several angles, the measured data can be used to fit coefficients in the model that correspond to the single-scattering albedo ϖ and the asymmetry factor g. Such a model can be used to infer ϖ and g of planetary surfaces and thereby potentially infer the composition and sizes of surface particles.

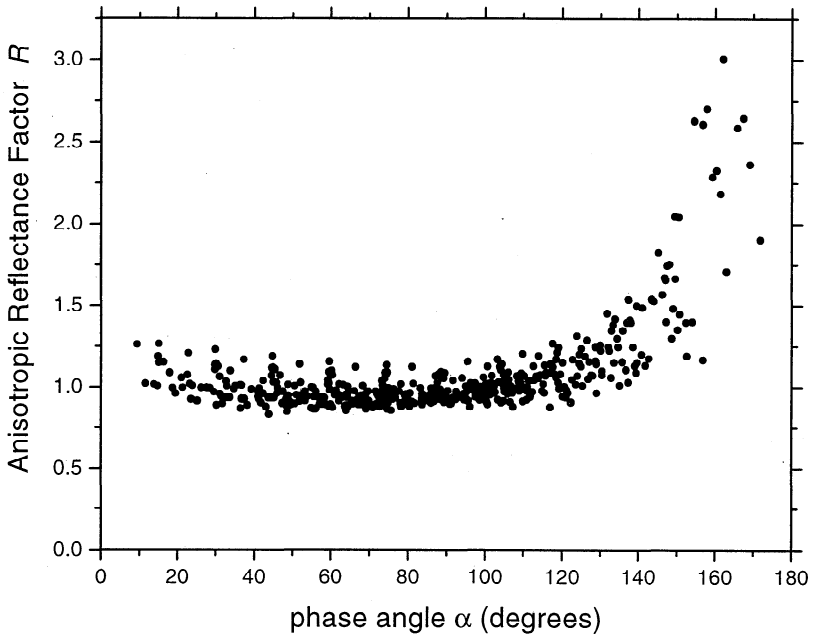

Figure 12. Anisotropic reflectance factor as a function of the phase angle α. Points for measured values at all combinations of angles (θ_o, θ_r, ϕ), but averaged over ϕ_{sas}, are plotted here, for the seven experiments marked with an asterisk in Table 1.

As a test of this procedure, the measurements of *Middleton and Mungall* [1952] for flat snow surfaces were analyzed by *Verbiscer and Veverka* [1990] and *Domingue et al.* [1997] in the context of Hapke's model. They inferred single-scattering co-albedo $(1-\varpi)\approx 0.006$ and $g\approx 0.6$, in contrast to the computations of Mic theory [*Wiscombe and Warren*, 1980], which gave $(1-\varpi)\approx 10^{-5}$ and $g\approx 0.89$ for visible light. Delta-Eddington-transformed values of the Mie results, after removing the diffraction peak as a δ function [*Joseph et al.*, 1976], are $(1-\varpi')\approx 5\times 10^{-5}$ and $g'\approx 0.47$. The results of Mie theory, incorporated into either δ-Eddington or discrete-ordinates multiple-scattering models, accurately explained the full course of albedo versus wavelength, from 0.3 μm to 2.5 μm, measured by *Grenfell et al.* [1994, Figure 4]. Empirical fits to the Hapke model are therefore apparently retrieving neither the untransformed nor the transformed single-scattering parameters. This could be due either to inaccuracies in the Hapke model or to experimental error by Middleton and Mungall, or both.

Verbiscer and Veverka [1990] and *Domingue et al.* [1997] have pointed out that the surfaces of some icy satellites in the outer Solar System exhibit enhanced backscattering, in contrast to the forward-scattering patterns observed for terrestrial snow. As discussed above in section 5.4, surface roughness could be an explanation for the enhanced backscattering, if the height-to-spacing ratios for roughness on those satellites are substantially greater than those for the sastrugi we observed. However, these authors instead interpreted the measurements as implying that the single-scattering phase function was itself backscattering ($g<0$).

Hapke's model was criticized by *Mishchenko* [1994] on the grounds that its application to these planetary observations often results in inferred $g<0$, whereas snow and soil particles are strongly forward-scattering at solar wavelengths. Mishchenko pointed out a number of defects in Hapke's model, as well as the ill-conditioned nature of the inverse problem for g, as possible explanations for retrievals of $g<0$. Furthermore, a backscattering bidirectional reflectance can be consistent with a large positive asymmetry factor, $g\approx 0.9$, if the surface contains macroscopic surface roughness, as shown in the models of *O'Rawe* [1991] and *Leroux and Fily* [this issue] cited above. *O'Rawe* [1991, Figures 5.15-5.28] showed that enhanced backscattering can occur not only for sastrugi but also for irregularity in the form of spherical hollows ("suncups") in snow, which have no preferred orientation in the horizontal plane. The fact that Verbiscer and Veverka were unable to obtain a backscattering bidirectional reflectance pattern using Hapke's model, even when a correction for surface roughness was included [*Hapke*, 1984], suggests that Hapke's model would not give the results obtained by O'Rawe.

Mishchenko and Macke [1997, Figures 13 and 14] also pointed out that Hapke's model violates energy conservation in that for a flat nonabsorbing surface with $g=0.8$ it predicts an albedo of 0.8 rather than the correct value 1.0. This disturbing result argues against the use of the Hapke model for interpreting measurements of snow reflectance.

The question remains whether surface roughness parameters such as sastrugi height, width, slope, spacing, and orientation can be inferred by measurements of reflected brightness. We have not investigated that question. If remote sensing of sastrugi parameters can be done, it will probably require a large number of observations at numerous combinations of the angles $(\theta_o, \theta_r, \phi)$. One aspect of the Antarctic climate that would make remote sensing of sastrugi parameters difficult is the frequent occurrence of blowing snow, which hides the sastrugi to some extent and reduces their influence on the planetary bidirectional reflectance.

8. Effect of Sastrugi on Albedo

Sastrugi not only alter the bidirectional reflectance pattern but also can reduce the albedo, for two reasons. First, when the Sun is low, the sides of sastrugi facing the Sun experience incidence at an angle smaller than the solar zenith angle, and increased irradiance relative to a flat surface. The sides facing away from the Sun receive less incident irradiance. The insolation-weighted average incidence angle is therefore reduced relative to that of a flat surface, and the albedo is reduced [*Warren*, 1982, Figures 10 and 12]. This effect also causes the albedo of a sastrugi field to depend on ϕ_{sas}. Both *Kuhn* [1974] and *Carroll and Fitch* [1981] measured broadband shortwave albedo at the South Pole to be greater by $\Delta A_s = 0.02$ for $\phi_{sas}=0^\circ$ than for $\phi_{sas}=90^\circ$. This effect is significant only under direct sunlight.

A second effect, which operates under both direct and diffuse illumination, is "trapping." Photons that reemerge from one side of a sastruga do not necessarily escape to space; they may be intercepted by the facing side of a neighboring sastruga and have another chance to be absorbed. The reduction in albedo by trapping depends on the albedo itself. Introducing roughness will cause no change to the albedo of a surface whose albedo when flat is 0.0 or 1.0. The greatest effect is for intermediate values of albedo; in the case of snow, this means near-infrared wavelengths. The visible and ultraviolet albedo of Antarctic snow is therefore scarcely affected by roughness, since it is so high, 0.96-0.98 [*Grenfell et al.*, 1994].

Four modeling studies have computed the effects of oriented surface roughness on snow albedo. *Carroll* [1982] modeled sastrugi as triangular wedges of specified slope, reflecting specularly (i.e., as mirrors) and illuminated by a direct beam. For the most extreme roughness he considered (60° slope; his Figure 9), the change in albedo ΔA_s from its flat-surface value of 0.83 varied with solar elevation h, from $\Delta A_s = 0$ at $h=23^\circ$ to $\Delta A_s = -0.17$ at $h=8^\circ$. These are averages over ϕ_{sas}. This latter large value of ΔA_s is unrealistic because at $h=8^\circ$ the incident radiation over a real snowfield is not a direct beam; it contains a large fraction of diffuse radiation due to Rayleigh scattering. Furthermore, most of the area of a sastrugied snow surface consists of slopes less than 60°.

Leroux and Fily [this issue] found that the sastrugi in their model, when illuminated from $h=23^\circ$, caused the albedo at $\lambda=900$ nm to drop from 0.90 for a flat surface to 0.85 at $\phi_{sas}=0^\circ$ and 0.81 at $\phi_{sas}=90^\circ$.

Pfeffer and Bretherton [1987] calculated the enhanced absorption of solar radiation by crevasses, effectively extending Carroll's work to steeper slopes because the geometry of their model (crevasses represented by wedge-shaped grooves) was similar. Their Figure 2 shows that for a surface whose albedo when flat is 0.8, the albedo is reduced by $\Delta A_s = -0.18$ for a crevasse-wall slope of 60°, in agreement with *Carroll* [1982], and by $\Delta A_s = -0.31$ for slopes of 80°.

O'Rawe [1991] computed the reduction of albedo due to sastrugi, and some of her results are plotted here. Figure 13a, for direct-beam incidence, shows how trapping becomes more

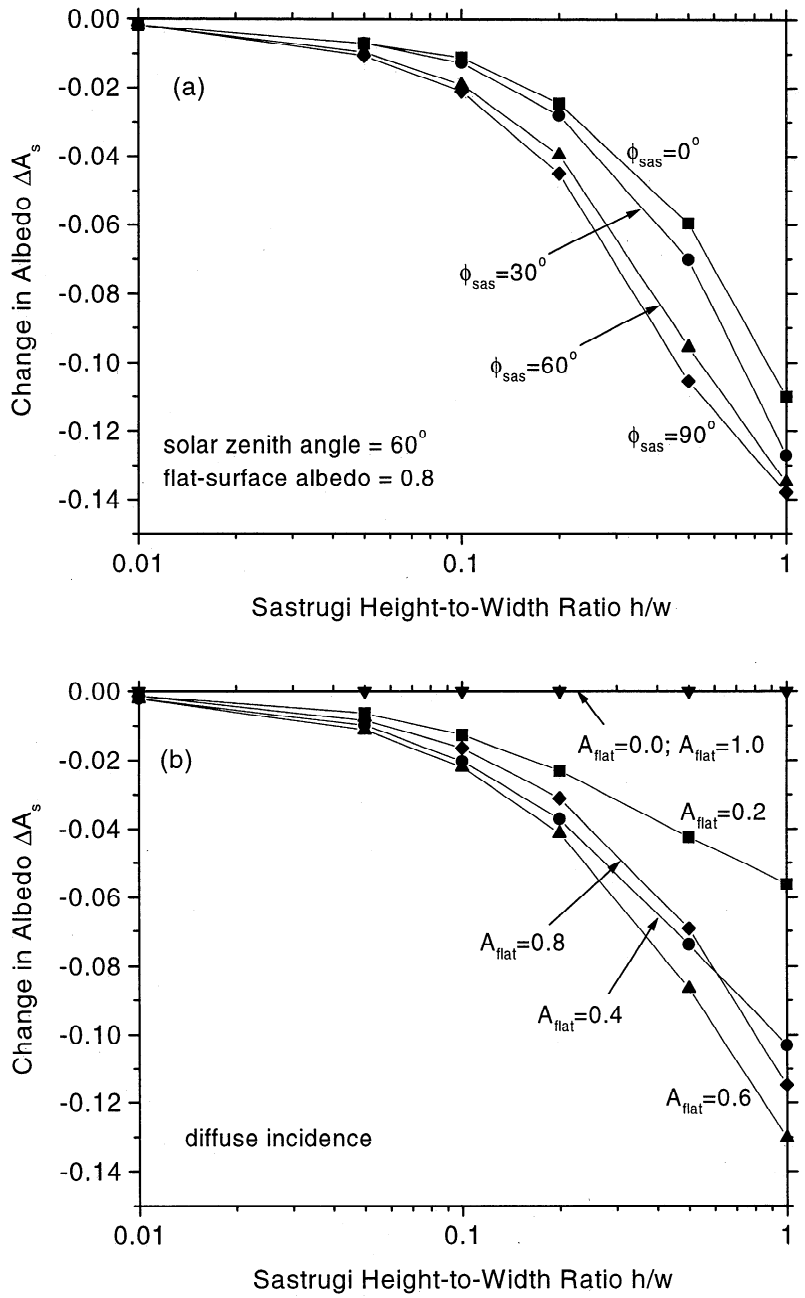

Figure 13. Effect of sastrugi on albedo, from the Monte-Carlo radiative transfer modeling of *O'Rawe* [1991]. Plotted is the change in albedo as a function of the height-to-width ratio of rectangular sastrugi with spacing equal to width (Figure 7). (a) Illumination by a direct beam at θ_o=60°, for four different sastrugi azimuths; flat-surface albedo = 0.8. (b) Under diffuse illumination, for four different values of flat-surface albedo at a reference incident zenith angle of 60°, corresponding to different wavelengths in the near-infrared. Data are taken from Figures 6.37f and 6.38 of *O'Rawe* [1991].

significant as the height-to-width ratio *h/w* increases, and also shows that the reduction of albedo due to alteration of the average incidence angle is greatest at ϕ_{sas}=90°. Figure 13b, for diffuse incidence, shows how the trapping effect is maximum at an intermediate value of flat-surface albedo (A_s = 0.6), and less for both higher and lower albedos (A_s = 0.4, A_s = 0.8). There is no effect for A_s = 0.0 or A_s = 1.0. For our sastrugi at the South Pole, with $h/w \approx 0.1$ but whose effects on R were seen to be modeled best by h/w=0.05, Figure 13 shows that a reduction in albedo of 0.00-0.01 (depending on wavelength) is achieved under diffuse illumination, and 0.01 under a direct beam at θ_o=60°. The reduction in albedo is greater at larger zenith angles, but the largest zenith angles do not contribute much to the surface energy budget. At the South Pole, only 3% of the annual incident solar energy is received at μ_o<0.1 (θ_o>84°) and only 13% at μ_o<0.2 (θ_o>78°); at other latitudes these percentages are even smaller [*Warren,* 1982].

9. Summary

The normal condition of snow in the polar regions is in the form of fields of sastrugi. Relative to a flat surface, sastrugi usually cause only a slight reduction in albedo but can alter

the bidirectional reflectance pattern significantly, particularly at large viewing angles and especially in the forward-scattering direction.

An experiment from a tower at the South Pole, where patterns of the anisotropic reflectance factor (R) can be measured at all relative azimuths between Sun and sastrugi over the course of a day, while the solar zenith angle remains unchanged, resulted in the following conclusions.

1. At visible wavelengths, as the solar elevation decreases there is more forward scattering until a solar elevation of around 10° is reached. At even lower solar elevations the pattern of reflected radiation becomes more isotropic as the diffuse fraction of the incident sunlight increases.

2. The R pattern at 660 nm is nearly identical to that at 900 nm and is probably nearly independent of wavelength from 300 to 900 nm. The R pattern is expected to become more anisotropic, with a relatively stronger forward peak, at near-infrared wavelengths longer than 900 nm, where snow is more absorptive.

3. The effect of sastrugi depends on the Sun-sastrugi azimuth angle ϕ_{sas}. A reduction in the forward peak results when ϕ_{sas}=90°; at oblique angles the R pattern shows left-right asymmetry across the principal plane.

4. Radiative transfer model calculations of R predict the effects of sastrugi to be larger than those observed, probably because of the idealized geometry (vertical walls) used in the models.

5. The variation of R with sastrugi orientation is 8% or less at θ_r <50°; we therefore recommend near-nadir viewing for accurate remote sensing over snow surfaces, where the sastrugi orientations and dimensions are in general not known. This recommendation is opposite that for remote sensing of broken clouds over dark surfaces. [θ_r =50° corresponds to a nadir angle of 42° for a typical polar-orbiting satellite at 900 km altitude.]

6. The experimental results for 600-660 nm wavelength have been parameterized by analytical functions of θ_0, θ_r, and ϕ, to allow computation of R at intermediate angles not measured in the experiment, but limited to $\theta_r \leq 50°$. This parameterization fits the daily average measurements to within 2% over a large range of angles, and to within 5% for most of the angular space. The parameterization is applicable to dry fine-grained snow with the surface roughness typically found on the Antarctic Plateau, and for solar elevations 0°-23°. Future measurements at lower-latitude Antarctic sites are needed to extend the parameterization to higher solar elevations. Because of the constancy of surface grain size on the Antarctic Plateau, this experiment was unable to investigate the variation of R with grain size.

7. A parameterization in terms of only one angle, the phase angle α between incoming and outgoing directions, cannot be expected to give the value of R to better than ±25%, even if limited to α<120°.

Our conclusions are probably valid for the entire East Antarctic Plateau. In the Slope region, however, larger sastrugi created by katabatic winds will cause more variation of R with ϕ_{sas} than we observed on the Plateau, and the viewing angle should probably be restricted to within 20° of nadir, as was done by *Doherty* [1997].

Our recommendation of near-nadir views for accurate remote sensing over snow is appropriate if the remote-sensing problem is to infer properties of the atmosphere [e.g., *Boime and Warren*, 1993] or the surface or planetary albedo. This recommendation is also appropriate for flat snow surfaces, where variations in crystal shape and orientation can cause the brightness to vary dramatically at large θ_r but not at small θ_r. For example, dark and light stripes have been observed in oblique views from aircraft on the West Antarctic ice streams, corresponding to the presence or absence of surface frost (N. Nereson, personal communication, 1996). On the other hand, for some purposes, it may be desirable to study the effects of these features rather than to avoid them, for example in the use of sastrugi to infer wind directions, in which case they may be best observed in oblique views.

Acknowledgments. Tom Grenfell and Peter Mullen helped with instrumentation and experimental design. Von Walden, Jarvis Belinne, Denise Worthen, and Robert Boime assisted with the field measurements. Other personnel at South Pole Station helped with deployment of the instrument, in particular, Rae Spain, Paul Mazure, Bill Getz, Paula McNerney, and Raymond Dunn. Dale Tysor and Ellsworth Dutton helped us access the NOAA-CMDL solar radiation measurements. Susan Harder helped with measurement of sastrugi dimensions. We thank Tom Grenfell, Gary Hansen, Catherine Leroux, and Norman Loeb for discussions, and Deborah Domingue and Michael Mishchenko for comments on the manuscript. Finally, we thank Austin Hogan for his efforts to have the meteorological tower erected at South Pole Station, which was essential for this experiment. This research was supported by National Science Foundation grants DPP-88-18570, OPP-91-20380, and OPP-94-21096.

References

Arakelian, T., Spectral and bidirectional reflectance of Antarctic snow, M.S. thesis, 84 pp., Calif. State Univ., Los Angeles, 1995.

Armstrong, T., B. Roberts, and C. Swithinbank, *Illustrated Glossary of Snow and Ice*, Scott Polar Res. Inst., Cambridge, England, 1966.

Bohren, C.F., *Clouds in a Glass of Beer*, John Wiley, New York, 1987.

Boime, R.D., and S.G. Warren, Mapping Antarctic ozone from visible-channel data, in *Atmospheric Ozone*, edited by T. Henriksen, *Proc. SPIE Int. Soc. Opt. Eng., 2047*, 122-131, 1993.

Brandt, R.E., T.C. Grenfell, and S.G. Warren, Optical properties of snow, *Antarct. J. U.S., 26(5)*, 272-275, 1991.

Carlson, R.W. and T. Arakelian, Spectral bidirectional reflectance and energy absorption rates of Antarctic snow, *Antarct. J. U.S., 28(5)*, 256-258, 1993.

Carroll, J.J., The effect of surface striations on the absorption of shortwave radiation, *J. Geophys. Res., 87*, 9647-9652, 1982.

Carroll, J.J., and B.W. Fitch, Dependence of snow albedos on solar elevation and cloudiness at the south pole, *J. Geophys. Res., 86*, 5271-5276, 1981.

Davies, R., Reflected solar radiances from broken cloud scenes and the interpretation of scanner measurements, *J. Geophys. Res., 89*, 1259-1266, 1984.

Dirmhirn, I., and F.D. Eaton, Some characteristics of the albedo of snow, *J. Appl. Meteorol., 14*, 375-379, 1975.

Doherty, S.J., The snow surface of the Antarctic Plateau as a calibration target for visible and ultraviolet channels on satellites, M.S. thesis, 89 pp., Univ. of Washington, Seattle, 1997.

Domingue, D., B. Hartman, and A. Verbiscer, The scattering properties of natural terrestrial snows versus icy satellite surfaces, *Icarus, 128*, 28-48, 1997.

Gow, A.J., On the accumulation and seasonal stratification of snow at the South Pole, *J. Glaciol., 5*, 467-477, 1965.

Grenfell, T.C., S.G. Warren, and P.C. Mullen, Reflection of solar radiation by the Antarctic snow surface at ultraviolet, visible, and near-infrared wavelengths, *J. Geophys. Res., 99*, 18,669-18,684, 1994.

Griggs, M., and W.A. Marggraf, Measurement of cloud reflectance properties and the atmospheric attenuation of solar and infrared energy, *Rep. AFCRL-68-003*, Air Force Cambridge Res. Lab., Bedford, Mass., 1967.

Han, W., K. Stamnes, and D. Lubin, Remote sensing of surface and cloud properties in the Arctic from AVHRR measurements, *J. Appl. Meteor.*, in press, 1998.

Hansen, J.E., and L.D. Travis, Light scattering in planetary atmospheres, *Space Sci. Rev., 16,* 527-610, 1974.

Hapke, B., Optical properties of the lunar surface, in *Physics and Astronomy of the Moon,* edited by Z. Kopal, pp. 155-211, Academic, San Diego, Calif., 1971.

Hapke, B., Bidirectional reflectance spectroscopy, 1, Theory, *J. Geophys. Res., 86,* 3039-3054, 1981.

Hapke, B., Bidirectional reflectance spectroscopy, 3, Correction for macroscopic roughness, *Icarus, 59,* 41-59, 1984.

Hapke, B., *Theory of Reflectance and Emittance Spectroscopy,* 455 pp., Cambridge Univ. Press, New York, 1993.

Joseph, J.H., W.J. Wiscombe, and J.A. Weinman, The delta-Eddington approximation for radiative flux transfer, *J. Atmos. Sci., 33,* 2542-2459, 1976.

Knap, W.H., and C.H. Reijmer, Anisotropy of the reflected radiation field over melting glacier ice: Measurements in Landsat-TM bands 2 and 4, *Remote Sens. Environ.,* in press, 1998.

Kuhn, M., Anisotropic reflection from sastrugi fields, *Antarct. J. U.S., 9(4),* 123-125, 1974.

Kuhn, M., Bidirectional reflectance of polar and alpine snow surfaces, *Ann. Glaciol., 6,* 164-167, 1985.

Kuhn, M., and L. Siogas, Spectroscopic studies at McMurdo, South Pole, and Siple stations during the austral summer 1977-78, *Antarct. J. U.S., 13(4),* 178-179, 1978.

LaChapelle, E.R., *Field Guide to Snow Crystals,* Univ. of Washington Press, Seattle, 1969.

Leroux, C., and M. Fily, Modeling the effect of sastrugi on snow reflectance, *J. Geophys. Res.,* this issue.

Li, S., A model for the anisotropic reflectance of pure snow, 60 pp., M.S. thesis, Univ. of Calif., Santa Barbara, 1982.

Lindsay, R.W., and D.A. Rothrock, Arctic sea ice albedo from AVHRR, *J. Clim., 7,* 1737-1749, 1994.

Lliboutry, L., The origin of penitents, *J. Glaciol., 2,* 331-338, 1954.

Mather, K.B., Further observations on sastrugi, snow dunes and the pattern of surface winds in Antarctica, *Polar Rec., 11,* 158-171, 1962.

McKee, T., and S.K. Cox, Simulated radiance patterns for finite cubic clouds, *J. Atmos. Sci., 33,* 2014-2020, 1976.

Middleton, W.E.K., and A.G. Mungall, The luminous directional reflectance of snow, *J. Opt. Soc. Am., 42,* 572-579, 1952.

Mishchenko, M.I., Asymmetry parameters of the phase function for densely packed scattering grains, *J. Quant. Spectrosc. Radiat. Trans., 52,* 95-110, 1994.

Mishchenko, M.I., and A. Macke, Asymmetry parameters of the phase function for isolated and densely packed spherical particles with multiple internal inclusions in the geometric optics limit, *J. Quant. Spectrosc. Radiat. Trans., 57,* 767-794, 1997.

Nayar, S.K., and M. Oren, Visual appearance of matte surfaces, *Science, 267,* 1153-1156, 1995.

O'Rawe, P., Monte Carlo models for the reflection of sunlight from rough snow surfaces: Suncups and sastrugi, M.S. thesis, 521 pp., Univ. of Washington, Seattle, 1991.

Parish, T.R., and D.H. Bromwich, The surface windfield over the Antarctic ice sheets, *Nature, 328,* 51-54, 1987.

Pfeffer, W.T., and C.S. Bretherton, The effect of crevasses on the solar heating of a glacier surface, in *The Physical Basis of Ice Sheet Modeling*, edited by E.D. Waddington and J. Walder, *IAHS Publ., 170,* 191-205, 1987.

Post, A., and E.R. LaChapelle, *Glacier Ice,* Univ. of Washington Press, Seattle, 1971.

Rhodes, J.J., R.L. Armstrong, and S.G. Warren, Mode of formation of "ablation hollows" controlled by dirt content of snow, *J. Glaciol., 33,* 135-139, 1987.

Steffen, K., Bidirectional reflectance of snow at 500-600 nm, in *Large Scale Effects of Seasonal Snow Cover*, edited by B. Goodison et al., *IAHS Publ., 166,* 415-425, 1987.

Stuhlmann, R., P. Minnis, and G.L. Smith, Cloud bidirectional reflectance functions: A comparison of experimental and theoretical results, *Appl. Opt., 24,* 396-401, 1985.

Suttles, J.T., R.N. Green, P. Minnis, G.L. Smith, W.F. Staylor, B.A. Wielicki, I.J. Walker, D.F. Young, V.R. Taylor, and L.L. Stowe, Angular radiation models for Earth-atmosphere system, Volume 1, Shortwave radiation, *NASA Ref. Pub. 1184,* National Aeronautics and Space Admin., Washington, D.C., 1988.

Tape, W., *Atmospheric Halos, Antarct. Res. Ser.,* vol. 64, 143 pp., AGU, Washington, D.C., 1994.

Taylor, V.R., and L.L. Stowe, Reflectance characteristics of uniform earth and cloud surfaces derived from Nimbus-7 ERB, *J. Geophys. Res., 89,* 4987-4996, 1984a.

Taylor, V.R., and L.L. Stowe, Atlas of reflectance patterns for uniform earth and cloud surfaces (Nimbus-7 ERB--61 days), *NOAA Tech. Rep. NESDIS 10,* Natl. Oceanic and Atmos. Admin., Washington, D.C., 1984b.

Verbiscer, A.J., and J. Veverka, Scattering properties of natural snow and frost: Comparison with icy satellite photometry, *Icarus, 88,* 418-428, 1990.

Warren, S.G., Optical properties of snow, *Rev. Geophys., 20,* 67-89, 1982.

Weller, G., The heat and mass balance of snow dunes on the central Antarctic Plateau, *J. Glaciol., 8,* 277-284, 1969.

Winther, J.-G., Spectral bi-directional reflectance of snow and glacier ice measured in Dronning Maud Land, Antarctica, *Ann. Glaciol., 20,* 1-5, 1994.

Wiscombe, W.J., and S.G. Warren, A model for the spectral albedo of snow, I, Pure snow, *J. Atmos. Sci., 37,* 2712-2733, 1980.

R.E. Brandt and S.G. Warren, Dept. of Atmospheric Sciences, Univ. of Washington, Box 351640, Seattle, WA 98195. (e-mail: brandt@atmos.washington.edu; sgw@atmos.washington.edu)

P. O'Rawe Hinton, Science Applications International Corporation, One Enterprise Parkway, Hampton, VA 23666. (e-mail: hinton@orawe.larc.nasa.gov)

(Received February 20, 1998; revised May 24, 1998; accepted June 1, 1998.)